Chapter 2

NONLINEAR FARADAY EFFECT AND ITS APPLICATIONS

Wojciech Gawlik [*] *and Szymon Pustelny* [†]
Center for Magneto-Optical Research,
M. Smoluchowski Institute of Physics, Jagiellonian University
Reymonta 4, 30-059 Kraków, Poland

Abstract

This chapter provides introduction to the important method of contemporary magneto-optics, the nonlinear Faraday effect. It starts with a theoretical background linking the nonlinearity of the effect with quantum coherences of atomic states. The discussion of methods enabling analytical and numerical calculation of nonlinear magneto-optical rotation are given. Next, Essential aspects of a typical experimental apparatus used for investigation of the effect are described. Finally, the most important applications of the phenomenon are reviewed, such as in magnetometry, nuclear magnetic resonance, magnetic resonance imaging, magnetic particle detection and quantum-state engineering.

1. Introduction

Nonlinear Faraday Effect (NFE) is a nonlinear magneto-optical phenomenon in which the light-induced coherences, i.e. quantum superpositions of Zeeman sublevels, of atoms constituting the sample contribute significantly to the rotation of the polarization-plane of a light propagating across the sample placed in a longitudinal magnetic field [1]. Early works in which the nonlinear polarization rotation was observed were the experiments with gas-lasers equipped with Brewster windows. Interplay between strong polarization anisotropy and NFE resulted in strong variations of laser output power with magnetic field [2, 3]. First more systematic studies of NFE were performed after the advent of tunable lasers which allowed working with atomic vapors close to their resonance frequency [4].

---

[*]E-mail address: gawlik@uj.edu.pl
[†]E-mail address: pustelny@uj.edu.pl

Both the linear Faraday Effect (LFE) and NFE allow applications to magnetometry but the latter offers much higher sensitivity. This sensitivity enhancement is one of the reasons why NFE attracts so much interest. Application of the effect for optical magnetometry was first suggested by Barkov *et al.* [5] and the idea has been verified experimentally by Budker and co-workers [6]. The authors demonstrated very high sensitivity of the magnetometric method for detection of a weak magnetic field within a narrow dynamic range around zero. These constraints were lessened with the introduction of a light modulation technique [7,8], as described in Sec. 4.1. It enabled measuring much stronger magnetic fields with ultra-high sensitivity.

The possibility of measuring nonzero magnetic fields with high sensitivity has already found its applications in several different fields. Applications include detection of magnetic micro- and nano-particles [9], nuclear magnetic resonance [10], and magnetic resonance imaging [11]. These applications are reviewed in Secs. 4.2.–4.4. of this chapter.

Another attractive and growing application of NFE is the quantum-state engineering. Just like long-living superpositions (coherences) of atomic states are essential for applications in high-sensitivity optical magnetometry, such superpositions are also a key element for quantum information. Therefore, the same experimental techniques which are used for control and modification of the coherences for NFE magnetometry are also useful for quantum information. These application of NFE for quantum state engineering are described in Sec 4.5. of this Chapter.

In the following sections we discuss main physical mechanisms of NFE and present the fundamentals of its theoretical description, describe typical experimental setup and discuss application of NFE.

2.   Theoretical Description of Nonlinear Faraday Effect

Theoretical description of NFE is performed using the density-matrix formalism. The knowledge of the matrix allows one to calculate the induced polarization $\mathbf{P}$ which characterizes the response of the medium to the electric field of light $\mathbf{E}$

$$\mathbf{P} = \mathrm{Tr}(\rho \mathbf{d}), \tag{1}$$

where $\mathbf{d}$ is the electric dipole moment operator. In our consideration, the matrix ρ is given in the mm' representation, where m and m' are the magnetic quantum numbers. In this representation, the populations and the coherences of the $|F, m\rangle$ atomic states, where F is the total angular momentum of an atom, are used to determine the overall quantum state of the system. Throughout this chapter it is assumed that the quantization axis is aligned with an external magnetic field. In such a case, the field shifts energies of the magnetic states $|F, m\rangle$ but does not mix them. Linearly polarized light propagates along the magnetic field and its polarization is perpendicular to the quantization axis. Therefore, the light is σ-polarized and can be decomposed into two circular components, the right- (σ^+) and left-handed (σ^-) components. We apply the convention in which the σ^+-polarized light generates transitions between magnetic sublevels of $\Delta m = 1$ and the σ^--polarized light of $\Delta m = -1$.

The evolution of the density matrix is described with the equation of motion [12]

$$\dot{\rho} = -\frac{i}{\hbar}\left[H, \rho\right] + \tilde{\Gamma}(\rho), \tag{2}$$

where H is the full Hamiltonian of the system (sum of the unperturbed Hamiltonian H_0 and the Hamiltonian of interaction V), $\tilde{\Gamma}$ is the operator describing relaxation and repopulation of the states, and $[\ ,\ ]$ denotes the commutator operator. Two approaches to solve Eq. (2) are presented in this chapter. In the first, perturbative approach, discussed in details in Sec. 2.1., the density matrix is expanded in a power series in the amplitude of the light field E and successive terms of the expansion are calculated iteratively. The approach is very useful because it enables analytical solutions and detailed analysis of the light-atom interaction, but it also has some limitations. One significant drawback of the method is its applicability to only weak and/or off-resonance interactions. In order to solve Eq. (2) for any light intensity and/or frequency, a nonperturbative approach is required. In the nonperturbative approach, a set of complex self-coupled equations, one for each density matrix element, needs to be evaluated precisely. Usually that cannot be done analytically and the equations need to be calculated numerically which is feasible for modern computers. However, the simplicity of the numerical approach is usually at the price of full understanding the physical background of the phenomena. The nonperturbative approach is discussed in Sec. 2.2.

2.1. Perturbative Approach

As discussed, for example, in Ref. [12], the density matrix ρ can be expanded in powers of the amplitude of electric field of light E

$$\rho = \sum_{n=0}^{\infty} \rho^{(n)} E^n. \tag{3}$$

Substituting Eq. (3) into Eq. (2) one can write a general relation for the density-matrix element $\rho_{\alpha\beta}$ in successive orders of perturbation

$$\dot{\rho}_{\alpha\beta}^{(n)} = -\frac{i}{\hbar}\left[H, \rho^{(n-1)}\right]_{\alpha\beta} + \tilde{\Gamma}\left(\rho^{(n)}\right)_{\alpha\beta}, \tag{4}$$

where superscript (n) indicates the n-th order of expansion. In the zeroth order of perturbation, i.e., in the absence of light, all atomic populations take their thermal equilibrium values and the density matrix consists only of diagonal elements representing the ground-state populations $\rho_{gg}^{(0)}$.[1] With no magnetic field, Zeeman sublevels of a given state are degenerate and equally populated. In the lowest-order of interaction, the off-diagonal elements $\rho_{ge}^{(1)}$ appear in the density matrix. These elements, called *optical coherences*, are associated with the linear susceptibility of a medium $\chi^{(1)}$, thus they determine linear absorption and dispersion. Once generated, the optical coherences evolve with time oscillating at a frequency which equals the unperturbed frequency of the transition ω_0 when atoms are not illuminated, or at the light frequency ω if the atoms interact with light (we assume $|\Delta\omega/\omega| \ll 1$, where

---

[1]It was assumed that the energy difference between the ground and excited state is big, e.g., of an optical range, thus the excited state is not populated in thermal equilibrium.

$\Delta\omega = \omega_0 - \omega$ is the detuning of the light from the transition). Within the second order of perturbation the excited-state populations $\rho_{ee}^{(2)}$ are generated. Additionally, the ground- and exited-state *Zeeman coherences*, described respectively with $\rho_{gg'}^{(2)}$ and $\rho_{ee'}^{(2)}$, are created. The Zeeman coherences oscillate at the frequency difference between the levels among which they are generated, thus the oscillations are much slower (from Hz to MHz) than those of optical coherences (on the order of 10^{14} Hz). At the second order of perturbation such phenomena as fluorescence and level-crossing can be described. In the next order of perturbation, the third-order optical coherences ($\rho_{ge'}^{(3)}$) can be calculated. As is shown below, the $\rho_{ge'}^{(3)}$ elements depend, among other quantities, on the ground-state Zeeman coherences, if such coherences can be generated in atoms. Within the third order, phenomena such as nonlinear absorption and dispersion, and hence NFE[2], as well as other optical phenomena like coherent population trapping [13], electromagnetically induced transparency [14] and absorption [15] can be explained. The fourth order of perturbation enables explanation of such phenomena as nonlinear fluorescence and nonlinear Hanle effect. Generally, processes which involve the first and second order of the density matrix expansion, namely $\rho^{(1)}$ and $\rho^{(2)}$, are considered as linear processes, while those related to higher orders are the nonlinear processes.

Successive terms of the perturbative expansion of the density matrix can be visualized graphically as shown in Fig. 1.
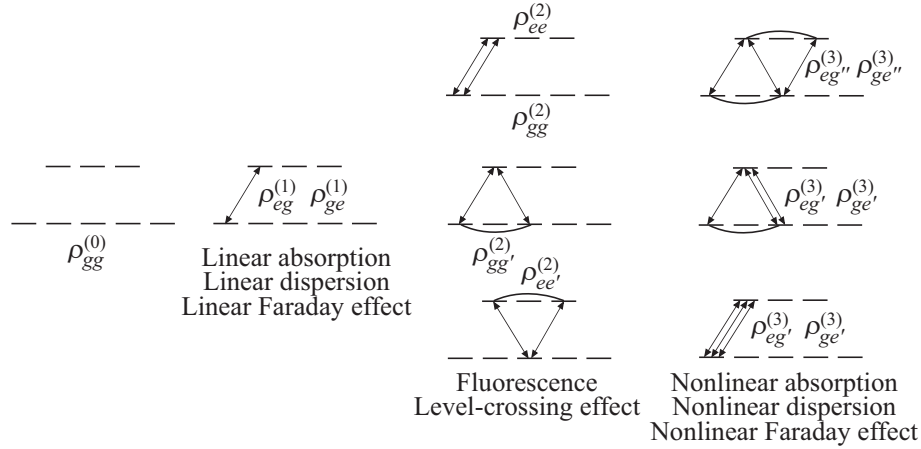

Figure 1. Visualization of the perturbative approach to the interaction of a two-level atom with an optical field. It is assumed that atomic levels have $F_g = 2$ and $F_e = 1$ and their degenerate magnetic sublevels are represented by horizontal bars. For a given order of perturbation the same subscript letters denote atomic populations or, if one of the letters is primed, the Zeeman coherences. Subscript letters e and g appearing together denote the optical coherences.

---

[2]Note that even if the coherences associated with the higher order of perturbation could contribute to NFE, their effect is usually much smaller than the third order contributions unless the light intensity is too high to justify the perturbative approach.

The basic system in which NFE can be analyzed is a three-level system, e.g., Λ, V. In this chapter we concentrate on the Λ system. That system can be realized by optical pumping on the $F_g = 1 \rightarrow F_e = 1$ transition with σ-polarized light. Optical pumping depletes the $m_g = 0$ sublevel and leaves whole atomic population in the $m_g = -1$ and $m_g = 1$ sublevels which, when interacting with the light, couple exclusively to the $m_e = 0$ sublevel. Since the $m_g = 0 \rightarrow m_e = 0$ transition is forbidden for $F_g = F_e$, a perfect Λ system is realized with $m_g = \pm 1$ and $m_e = 0$ sublevels.. The familiar $F_g = 1 \rightarrow F_e = 0$ system also approximates the Λ-system, if one neglects the $m_g = 0$ sublevel.

In order to theoretically describe NFE for a specific atomic system, for instance, the Λ system interacting with light and magnetic field, the general form of the total Hamiltonian H [Eq. (4)] is taken

$$H = H_0 + V = H_0 - \mathbf{E} \cdot \mathbf{d} - \boldsymbol{\mu} \cdot \mathbf{B} \tag{5}$$

where $\boldsymbol{\mu}$ is the magnetic dipole-moment operator. Unfortunately, Eq. (4) cannot be solved exactly for a real light field represented as

$$\mathbf{E} = \mathbf{e}_+ E \cos \omega t + \mathbf{e}_- E \cos \omega t, \tag{6}$$

where $\mathbf{e}_+$, $\mathbf{e}_-$ are the right- and left-handed unit vectors. This can be done, however, in the so-called rotating wave approximation wherein light is written in a complex form

$$\mathbf{E} = \mathbf{e}_+ E e^{-i\omega t} + \mathbf{e}_- E e^{-i\omega t}. \tag{7}$$

Combining Eqs. (4), (5), and (7), one obtains a set of equations for all density matrix elements in a given order of perturbation

$$
\begin{aligned}
\dot{\rho}_{--}^{(n)} &= -i\Omega \left(\rho_{-0}^{(n-1)} - \rho_{0-}^{(n-1)} \right) - \gamma \left(\rho_{--}^{(n)} - \rho_{--}^{(0)} \right), \\
\dot{\rho}_{++}^{(n)} &= -i\Omega \left(\rho_{+0}^{(n-1)} - \rho_{0+}^{(n-1)} \right) - \gamma \left(\rho_{++}^{(n)} - \rho_{++}^{(0)} \right), \\
\dot{\rho}_{00}^{(n)} &= i\Omega \left(\rho_{+0}^{(n-1)} - \rho_{0+}^{(n-1)} + \rho_{-0}^{(n-1)} - \rho_{0-}^{(n-1)} \right) - \Gamma \rho_{00}^{(n)}, \\
\dot{\rho}_{0-}^{(n)} &= -i\Omega \left(\rho_{00}^{(n-1)} - \rho_{--}^{(n-1)} - \rho_{+-}^{(n-1)} \right) - i \left(\omega_0 + \omega_L - i\Gamma_{coh} \right) \rho_{0-}^{(n)}, \\
\dot{\rho}_{0+}^{(n)} &= -i\Omega \left(\rho_{00}^{(n-1)} - \rho_{++}^{(n-1)} - \rho_{-+}^{(n-1)} \right) - i \left(\omega_0 - \omega_L - i\Gamma_{coh} \right) \rho_{0+}^{(n)}, \\
\dot{\rho}_{-+}^{(n)} &= -i\Omega \left(\rho_{-0}^{(n-1)} - \rho_{0+}^{(n-1)} \right) + i \left(2\omega_L + i\gamma_{coh} \right) \rho_{-+}^{(n)},
\end{aligned}
\tag{8}
$$

where the $\pm$ and 0 subscripts denote the states with $m_g = \pm 1$ and $m_e = 0$, respectively, $\Omega = Ed/\hbar$ is the Rabi frequency, $\omega_L = g\mu_B B/\hbar$ the Larmor frequency with μ_B being the Bohr magneton, g the Landé factor, and B the strength of the magnetic field, γ and Γ are the relaxation rates of the ground- and excited-state populations, respectively, Γ_{coh} the relaxation rate of the optical coherence and γ_{coh} the relaxation rate of the ground-state Zeeman coherences[3].

_____

[3]For the sake of simplicity, it was assumed that the excited state does not relax to the ground state but deexcites to the other, uncoupled state. In such a case of an open system, the equations for $\dot{\rho}_{\pm\pm}^{(n)}$ do not depend on $\dot{\rho}_{00}^{(n)}$, i.e., there is no ground-state repopulation.

As discussed above, for nearly resonant light ($\Delta\omega \ll \omega$) optical coherences oscillate at the frequency ω. Therefore, in order to separate the fast oscillations of the coherences from much slower variation of their amplitudes, the slowly varying envelope $\sigma_{\alpha\beta}$ of the optical coherence $\rho_{\alpha\beta}$ is introduced

$$\rho_{\alpha\beta}(t) = \sigma_{\alpha\beta}(t)e^{-i\omega t}. \tag{9}$$

Introduction of $\sigma_{\alpha\beta}$ allows one to calculate the steady-state solution of Eqs. (8), i.e., the solution that is valid long after all transients associated with the light turn-on have died out. This solution is obtained by setting the left-hand side of Eqs. (8) equal to zero and the equations become

$$
\begin{aligned}
\rho_{--}^{(n)} &= \rho_{--}^{(0)} - \frac{i\Omega}{\gamma}\left(\sigma_{-0}^{(n-1)} - \sigma_{0-}^{(n-1)}\right), \\
\rho_{++}^{(n)} &= \rho_{++}^{(0)} - i\frac{\Omega}{\gamma}\left(\sigma_{+0}^{(n-1)} - \sigma_{0+}^{(n-1)}\right), \\
\rho_{00}^{(n)} &= \frac{i\Omega}{\Gamma}\left(\sigma_{+0}^{(n-1)} - \sigma_{0+}^{(n-1)} + \sigma_{-0}^{(n-1)} - \sigma_{0-}^{(n-1)}\right), \\
\sigma_{0-}^{(n)} &= -\frac{\Omega}{A_-}\left(\rho_{00}^{(n-1)} - \rho_{--}^{(n-1)} - \rho_{+-}^{(n-1)}\right), \\
\sigma_{0+}^{(n)} &= -\frac{\Omega}{A_+}\left(\rho_{00}^{(n-1)} - \rho_{++}^{(n-1)} - \rho_{-+}^{(n-1)}\right), \\
\rho_{-+}^{(n)} &= \frac{\Omega}{2\omega_L + i\gamma}\left(\sigma_{-0}^{(n-1)} - \sigma_{0+}^{(n-1)}\right),
\end{aligned}
\tag{10}
$$

where $A_\pm = \Delta\omega \mp \omega_L - i\Gamma/2$, $\gamma_{coh} = \gamma$ and $\Gamma_{coh} = (\Gamma + \gamma)/2 \approx \Gamma/2$ for $\Gamma \gg \gamma$.

Explicit forms of the density-matrix elements calculated up to the third order of perturbation are shown in Table 1. Comparison of $\sigma_{0\pm}^{(1)}$ and $\sigma_{0\pm}^{(3)}$ reveals differences between linear and nonlinear optical processes. The first-order optical coherences $\sigma_{0\pm}^{(1)}$ are characterized with complex Lorentz functions. The widths of the associated dispersive and absorptive curves corresponding to the real and imaginary parts of $\sigma_{0\pm}^{(1)}$, respectively, are given by the relaxation rate of the optical coherences $\Gamma/2$, while the amplitudes of the contributions depend linearly on the amplitude of the light electric field ($\sigma_{0\pm}^{(1)} \propto \Omega$). Third-order coherences $\sigma_{0\pm}^{(3)}$ take more complicated forms than $\sigma_{0\pm}^{(1)}$. Not only are they characterized with a linear combination of several Lorentz functions of the width $\Gamma/2$ but also they acquire additional contribution associated with the ground-state Zeeman coherences. This contribution has much narrower width, which is determined by the relaxation rate of ground-state coherences γ ($\gamma \ll \Gamma$) and amplitude depending in a nonlinear way on the electric light field ($\sigma_{0\pm}^{(3)} \propto \Omega^3$). It is noteworthy that for very small γ the feature associated with ground-state coherences has very strong dependence on magnetic field which makes it attractive for magnetometric applications (Sec. 4.1.).

In Fig. 2, the real and imaginary parts of the first- $\sigma_{0+}^{(1)}$ and third-order $\sigma_{0+}^{(3)}$ optical coherences are shown as functions of the magnetic field. The plots reveal differences between the linear and nonlinear dispersion and absorption, in particular, the narrow contribution associated with the ground-state Zeeman coherences.

The perturbative approach yields relatively simple analytical formulae for different density matrix elements. These forms allow one to study various processes associated with

Table 1. Density matrix elements calculated for a given order of perturbation. It was assumed that there are three equally populated levels in the ground state $N/3$, where N is the number of atoms.

Perturbation order	Density matrix element
0	$\rho_{gg}^{(0)} = \frac{N}{3}$
1	$\sigma_{0\pm}^{(1)} = \frac{\Omega N}{2A_{\pm}}$
2	$\rho_{\pm\pm}^{(2)} = \frac{N}{3}\left[1 - \frac{i\Omega^2}{\gamma}\left(\frac{1}{A_{\pm}^*} - \frac{1}{A_{\pm}}\right)\right]$ $\rho_{00}^{(2)} = \frac{i\Omega^2 N}{2\Gamma}\left(\frac{1}{A_-^*} - \frac{1}{A_-} + \frac{1}{A_+^*} - \frac{1}{A_+}\right)$ $\rho_{-+}^{(2)} = \frac{\Omega^2 N}{2(2\omega_L + i\gamma)}\left(\frac{1}{A_-^*} - \frac{1}{A_+}\right)$
3	$\sigma_{0\pm}^{(3)} = \frac{\Omega N}{3A_{\pm}}\left[1 - \frac{i\Omega^2}{\gamma}\left(\frac{1}{A_{\pm}^*} - \frac{1}{A_{\pm}}\right) - \frac{i\Omega^2}{\Gamma}\left(\frac{1}{A_{\mp}^*} - \frac{1}{A_{\mp}}\right) + \right.$ $\left. + \frac{\Omega^2}{2\omega_L - i\gamma}\left(\frac{1}{A_{\pm}} - \frac{1}{A_{\mp}^*}\right)\right]$

light-atom interaction, and in such a way as to point out the differences between linear and nonlinear optical processes. One significant limitation of the approach is its applicability to low light-intensity and/or off-resonance interactions only. An additional drawback lies in the usage of the steady-state approximation which does not allow the dynamics of the process to be analyzed. These problems, however, can be addressed using the approach discussed in the following section.

2.2. Nonlinear Faraday Effect as a Three-Stage Process

Consideration of nonlinear optical phenomena as three-stage processes is a useful way of describing these effects. In such an approach, light first modifies medium properties by redistributing populations and generating coherences between atomic or molecular levels (the pumping stage) which then evolve under interaction with external fields leading to further change of medium properties (the probing stage). Finally, the medium affects the light (the probing stage) which depends also on the properties of the light. Despite the fact that usually all these stages occur simultaneously, the three-stage approach facilitates understanding of the nonlinear optical effects.

As discussed above, in the most general case, Eq. (2) describing the density matrix evolution cannot be solved analytically. Hence, in order to obtain exact solution of the equation one needs to apply numerical methods. In that case it is very useful to visualize the matrix ρ which facilitates study of its time evolution. The method described, for example, in Ref. [16] enables representation of the matrix in a form of a 3D surface[4] whose distance

---

[4]It should be noted that numerical and graphical representations of the density matrix are fully equivalent; for a given density matrix a specific surface can be drawn and a given surface enables extraction of the numerical form of the density matrix.
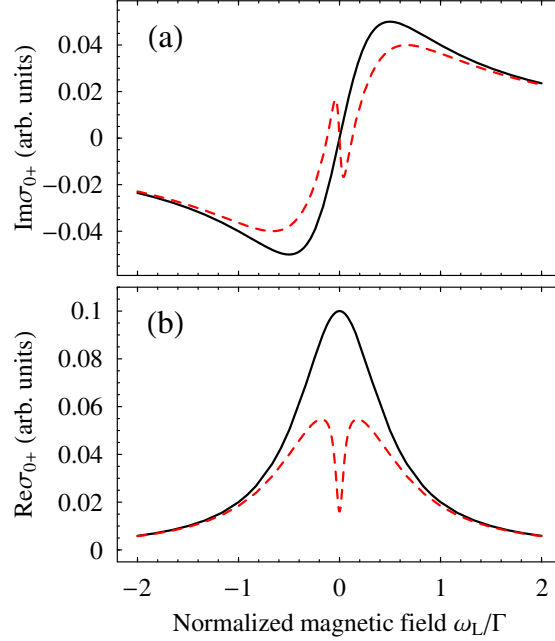
Figure 2. Comparison of real (a) and imaginary (b) parts of the optical coherences calculated in the first ($\sigma_{0+}^{(1)}$) (solid lines) and third ($\sigma_{0+}^{(3)}$) order of perturbation (broken lines).

from the origin in a given direction $r(\theta, \alpha)$ corresponds to

$$r(\theta, \alpha) = R^{-1}(\alpha, \theta, 0)\rho R(\alpha, \theta, 0)|_{FF}, \tag{11}$$

where $|_{FF}$ denotes the projection with the highest m and $R(\alpha, \theta, 0)$ is the quantum-mechanical rotation operator [17] in spherical coordinates, while θ and α denote the azimuthal and polar angles, respectively. Below we applied the method to analyze evolution of the density matrix during pumping, evolution, and probing stages in the nonlinear Faraday effect.

A sample of unpolarized Λ-type atoms, i.e., atoms equally populated in all ground-state sublevels, interacts with a linearly polarized light in the absence of a magnetic field. Under such conditions the density matrix was evaluated numerically using Eq. (2) and visualized with the method discussed above. The successive phases of the pumping stage are shown in Fig. 3. The light repopulates atomic levels and generates coherences among them which manifest as a change of the 3D surface used for the matrix visualization. The surface shape evolves from a symmetric sphere [Fig. 3(a)] to an anisotropic, peanut-like shape [Fig. 3(d)]. The axis of the induced density-matrix anisotropy, and hence the axis of the associated optical anisotropy of atoms, is aligned with the light polarization.

Application of the magnetic field causes evolution of the pumped-atom density matrix [Fig. 4(a)] which manifests as the rotation of the peanut-like shape around the field (the Larmor precession) [Fig. 4(a)-(e)]. During the rotation a number of pumped atoms decreases
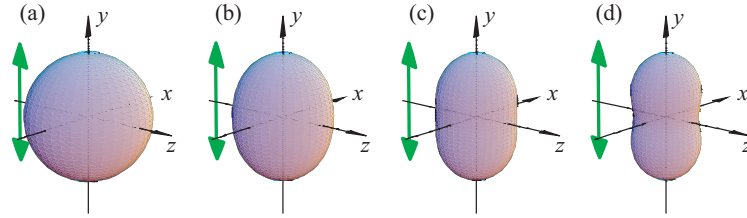
Figure 3. Pumping stage: subsequent phases of density-matrix evolution (a)-(d) under inter-action with linearly polarized light (light polarization along y). The initially isotropic distribution of atomic angular momenta (a) evolves toward an anisotropic, peanut-like shape whose axis is aligned along light polarization (d).

due to relaxation which is seen as deterioration of the peanut-like shape amplitude (only density-matrix contribution associated with pumped atoms is shown in Fig. 4). Simultaneously with the precession and relaxation, light is continuously pumping new atoms of optical anisotropy axis aligned along its polarization. Anisotropy axes of all these atoms precess in the field, all with different phases. As a result, atoms described with density matrices corresponding to differently spatially oriented "peanuts" of different amplitudes coexist in the medium [Fig. 4(e)].
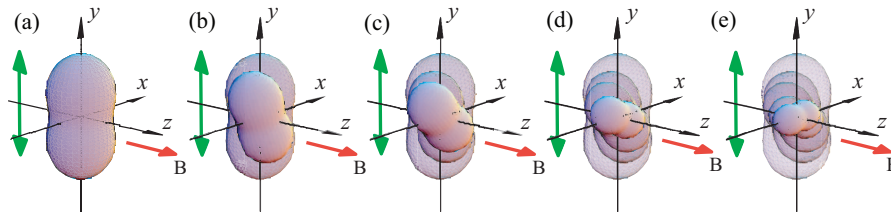

Figure 4. Evolution stage: subsequent phases (a)-(e) of the density-matrix evolution under interaction with y-polarized CW light and nonzero magnetic field $\vec{B}$. The initially pumped atoms precess in the field and relax in time which is seen as the rotation of the "peanut" and decrease of its amplitude over time (contribution from pumped atoms are only shown). Simultaneously with these processes, CW light pumps new atoms. The precessing atoms accumulate different phases than the atoms pumped earlier or later. As a result, atoms with all spatial orientations of the anisotropy axes exist in the medium (e).

Pumping, precession, and relaxation lead to creation of a net macroscopic anisotropy of the medium. In order to calculate this anisotropy, one needs to integrate over density matrices of all atoms existing in the medium. That may be reduced to simple averaging over all spatial orientations of corresponding 3D surfaces. The averaging results in appearance of a net 3D surface (Fig. 5) and hence macroscopic optical anisotropy of the medium with the axis orientation depending on the magnetic field, relaxation rate, and electric field of light.
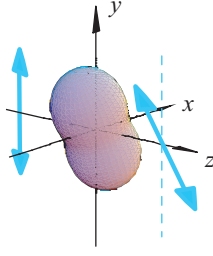
Figure 5. Net anisotropy of the medium generated under interaction with the linearly y-polarized light polarized light and the magnetic field directed along z. The orientation of the anisotropy is determined by the magnetic field, the rate of relaxation of atomic polarization and the light intensity.

Finally, the optical anisotropy of the medium is analyzed with the probe light[5]. In general, the axis of that anisotropy is not aligned along the the probe-light polarization so the medium is birefringent for the light. It results in the rotation of its polarization upon propagation through the medium. Since, as it was shown earlier, net polarization of the medium depends, among other quantities, on the pumping light intensity, the rotation of the probe-light polarization is also its function. This light-intensity dependence of the rotation is thus the main signature of nonlinear nature of this effect.

As shown, the visual approach is a very powerful and useful tool to describe of nonlinear optical phenomena. It allows NFE to be presented in a simple and intuitive way. Its important advantage over perturbative approach is the ability to describe a number of interesting, especially dynamic, effects.

2.3.   Calculation of the Polarization-Plane Rotation

In the two preceding subsections, the methods of evaluation of the density matrix were discussed. As shown in Eq. (1), the knowledge of the matrix allows one to calculate the induced polarization $\mathbf{P}$. Complex amplitude P of the induced polarization $\mathbf{P}$

$$\mathbf{P} = \hat{e}_E P e^{-i\omega t}, \tag{12}$$

where $\hat{e}_E$ is the unit vector along light polarization, enables formulation of the relation between the polarization amplitude P and the amplitude of the electric field of light E

$$P = \epsilon_0 \chi_{eff} E, \tag{13}$$

---

[5]In many experimental arrangements pumping and probing is performed with the same light beam – the so-called single-beam arrangement.

with ϵ_0 being the electric permittivity of free space and χ_{eff} the effective electric suscepti-bility of the medium[6]. Using Eqs. (1), (12), and (13), one can show that

$$\chi_{eff} = \frac{\sum_{eg} d_{eg}\rho_{ge}}{E}, \tag{14}$$

where d_{eg} is the dipole moment of a transition between states e and g. The susceptibility of a medium is related to the relative permittivity ϵ_r by

$$\epsilon_r = 1 + \chi_{eff}. \tag{15}$$

The complex refractive index η can be calculated through the relation

$$\eta = n + i\kappa = \sqrt{\epsilon_r} = \sqrt{1 + \chi_{eff}} \approx 1 + \frac{1}{2}\chi_{eff}, \tag{16}$$

where n is the refractive index, κ denotes the absorption coefficient, and it was assumed that $\chi_{eff} \ll 1$ which is true for low density atomic vapors. Combining Eqs. (14) and (16), one can write relations for the refractive index n and the absorption coefficient κ

$$n = 1 + \mathrm{Re}\frac{\sum_{eg} d_{eg}\rho_{ge}}{2E},$$
$$\kappa = \mathrm{Im}\frac{\sum_{eg} d_{eg}\rho_{ge}}{2E}. \tag{17}$$

For the considered Λ-type atoms, the nonzero magnetic field removes degeneration of the ground-state sublevels which differentiates the complex refractive indices, $\eta_+ \neq \eta_-$, of the two circular polarizations σ^+ and σ^-, respectively. A result of this light-induced birefringence is that each of the circular components of linearly polarized light propagate in the medium with different velocities, so after a sample of length l the accumulated phase difference $\Delta\varphi$ is

$$\Delta\varphi = \frac{\omega l}{c}\left(n_+ - n_-\right). \tag{18}$$

The phase difference $\Delta\varphi$ causes rotation of the polarization plane of linearly polarized light by the angle ϕ

$$\phi = \frac{\Delta\varphi}{2} = \frac{\omega l}{2c}\left(n_+ - n_-\right) = \frac{\omega l}{4Ec}\sum_{eg}\left[d_{eg}\rho_{ge}\delta_{m_e-m_g,1} - d_{eg}\rho_{ge}\delta_{m_e-m_g,1}\right], \tag{19}$$

where $\delta_{x,y}$ is the Kronecker delta function. Equation (19) allows the rotation of the polar-ization plane of linearly polarized light to be calculated using the density matrix formalism.

---

[6]Typically in perturbative nonlinear optics, the amplitude of induced polarization P is defined as $P = \epsilon_0\Sigma_{n=1}^{\infty}\chi^{(n)}E^n$, where $\chi^{(n)}$ is the n-th order electric susceptibility. For that definition, all $\chi^{(n)}$ are independent of the electric field E. By comparing this definition with Eq. (13), one finds that the effective electric susceptibility $\chi_{eff} = \Sigma_{n=1}^{\infty}\chi^{(n)}E^{(n-1)}$ is light dependent.

2.4. Nonlinear Faraday Effect with Modulated Light

There are several techniques of light modulation that can be applied for synchronous pumping of atoms. The one described in this chapter employs amplitude modulation of the pumping light. More information on other techniques, in particular frequency modulation of light, can be found in Refs. [18–20].

In order to account for amplitude modulation of light, Eq. (7) describing the electric field of light in rotating-wave approximation needs to be rewritten into the form

$$
\begin{aligned}
\mathbf{E} &= \left(\mathbf{e}_+ E e^{-i\omega t} + \mathbf{e}_- E e^{-i\omega t}\right)\left[1 + a_m \cos(\Omega_m t)\right] = \\
&= \mathbf{e}_+ E \left(e^{-i\omega t} + \frac{a_m}{2} e^{-i(\omega - \Omega_m)t} + \frac{a_m}{2} e^{-i(\omega + \Omega_m)t}\right) - \\
&- \mathbf{e}_- E \left(e^{-i\omega t} + \frac{a_m}{2} e^{-i(\omega - \Omega_m)t} + \frac{a_m}{2} e^{-i(\omega + \Omega_m)t}\right),
\end{aligned}
\tag{20}
$$

where Ω_m is the modulation frequency and a_m the numerical factor responsible for the modulation depth ($a_m \in (0, 1]$). As seen, amplitude modulation of light leads to a change of light spectrum which, in addition to the carrier frequency, consists of two sidebands at $\omega - \Omega_m$ and $\omega + \Omega_m$ of the amplitudes $a_m/2$. Substituting Eq. (20) into Eq. (2) enables the calculation of the density matrix of atoms interacting with amplitude-modulated light. In such a case, however, the rotating-wave approximation does not allow one to fully extract time dependence from the density-matrix equation of motion. Due to this reason, matrix ρ is expanded into a Fourier series over the modulation frequency Ω_m

$$
\rho = \sum_{k=-\infty}^{\infty} \rho^{[k]} e^{ik\Omega_m t},
\tag{21}
$$

where $\rho^{[k]}$ is the k-th Fourier coefficient. Using the Fourier expansion of the density matrix and collecting terms oscillating at the same frequencies ($r\Omega_m$, where r is the integer) one

obtains the infinite set of self-coupled equations

$$
\begin{aligned}
\rho_{--}^{[k]} &= \rho_{--}^{(0)}\delta_{0,k} - \frac{i\Omega}{\gamma}\left[\sigma_{-0}^{[k]} - \sigma_{0-}^{[k]} + \frac{a_m}{2}\left(\sigma_{-0}^{[k-1]} - \sigma_{0-}^{[k-1]} + \sigma_{-0}^{[k+1]} - \sigma_{0-}^{[k+1]}\right)\right], \\
\rho_{++}^{[k]} &= \rho_{++}^{(0)}\delta_{0,k} - \frac{i\Omega}{\gamma}\left[\sigma_{+0}^{[k]} - \sigma_{0+}^{[k]} + \frac{a_m}{2}\left(\sigma_{+0}^{[k-1]} - \sigma_{0+}^{[k-1]} + \sigma_{+0}^{[k+1]} - \sigma_{0+}^{[k+1]}\right)\right], \\
\rho_{00}^{[k]} &= \frac{i\Omega}{\Gamma}\left[\sigma_{+0}^{[k]} - \sigma_{0+}^{[k]} + \sigma_{-0}^{[k]} - \sigma_{0-}^{[k]} + \frac{a_m}{2}\left(\sigma_{+0}^{[k-1]} - \sigma_{0+}^{[k-1]} + \sigma_{-0}^{[k-1]} - \sigma\rho_{0-}^{[k-1]}+\right.\right. \\
&\qquad\left.\left. + \sigma_{+0}^{[k+1]} - \sigma_{0+}^{[k+1]} + \sigma_{-0}^{[k+1]} - \sigma_{0-}^{[k+1]}\right)\right], \\
\sigma_{0-}^{[k]} &= -\frac{\Omega}{A_-}\left[\rho_{00}^{[k]} - \rho_{--}^{[k]} - \rho_{+-}^{[k]} + \frac{a_m}{2}\left(\rho_{00}^{[k-1]} - \rho_{--}^{[k-1]} - \rho_{+-}^{[k-1]}+\right.\right. \\
&\qquad\qquad\qquad\left.\left. + \rho_{00}^{[k+1]} - \rho_{--}^{[k+1]} - \rho_{+-}^{[k+1]}\right)\right], \\
\sigma_{0+}^{[k]} &= -\frac{\Omega}{A_+}\left[\rho_{00}^{[k]} - \rho_{++}^{[k]} - \rho_{-+}^{[k]} + \frac{a_m}{2}\left(\rho_{00}^{[k-1]} - \rho_{++}^{[k-1]} - \rho_{-+}^{[k-1]}+\right.\right. \\
&\qquad\qquad\qquad\left.\left. + \rho_{00}^{[k+1]} - \rho_{++}^{[k+1]} - \rho_{-+}^{[k+1]}\right)\right], \\
\rho_{-+}^{[k]} &= \frac{\Omega}{2\omega_L + i\gamma}\left[\sigma_{-0}^{[k]} - \sigma_{0+}^{[k]} + \frac{a_m}{2}\left(\sigma_{-0}^{[k-1]} - \sigma_{0+}^{[k-1]} + \sigma_{-0}^{[k+1]} - \sigma_{0+}^{[k+1]}\right)\right].
\end{aligned}
$$

$$(22)$$

New terms arising in relations for $\rho^{[k]}$ appear due to coupling between the $[k-1]$ and $[k+1]$ density-matrix elements with the sidebands $\omega - \Omega_m$ and $\omega + \Omega_m$ and the strength of this coupling is determined by parameter a_m.

In general, evolution of the density-matrix elements given by Eqs. (22), requires solution of an infinite number of the self-coupled equations. In practice, however, the series given by Eq. (21) is replaced by a finite Fourier series with the cut-off at k_c, i.e., for $|k| > k_c$ $\rho^{[k]} \equiv 0$. Such an approximation is valid because $k-1$-th and $k+1$-th order elements of the density matrix contribute to $\rho^{[k]}$ by, at most, half of the contribution from different k-th order elements of the matrix; the higher-order coefficients reflect response of a medium to higher harmonics of the modulation frequency which are weaker than that to the lower ones. Due to this fact, it is usually enough to truncate the Fourier expansion of the density matrix at $k = 7$.

The idea of synchronous pumping of atoms, which is fundamental for NFE with modulated light, can be easily understood using the density-matrix visualization method. In Fig. 6 subsequent phases of pumping with amplitude-modulated light are shown. At time $\tau = 0$ [Fig. 6(a)], the atoms are pumped by the light and the peanut-like density matrix is generated. Similarly to the CW case, the "peanut" rotates in the magnetic field (a)-(e) but in this case the rotation occurs with strongly attenuated or completely turned off pumping light. The light is on again when the peanut-like density matrix is rotated by 180° [Fig. 6(a)], that is, at time $\tau = \pi/\omega_L$. In such a case, the anisotropy axis of newly pumped atoms is aligned with the axis of atoms pumped earlier. If the precession frequency ω_L is much faster than the relaxation rate γ, the decrease of the "peanut" amplitude in a single pumping-precession cycle is negligible and eventually most of the atoms precess in the field with the same phase. This leads to generation of macroscopic dynamic anisotropy of the
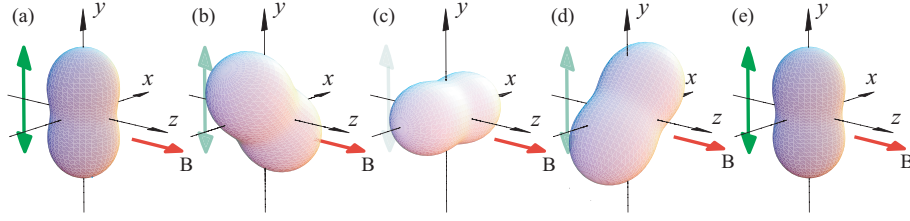
Figure 6. Visualization of interaction of amplitude-modulated light (polarization along y) with atoms subjected to the magnetic field $\vec{B}$ directed along z. If the pumping frequency ω_m is synchronized with the Larmor frequency ω_L (see text), the anisotropy axes of the atoms pumped during the different pumping cycles are aligned and the macroscopic dynamic polarization of the medium is generated. Time dependence of the amplitude-modulated light intensity is illustrated by different shading of the double-head arrows which mark oscillations of the light electric vector.

medium whose anisotropy axis rotates in time. This results in the time-dependent rotation of the polarization plane of unmodulated probe light propagating through the medium at twice the Larmor frequency[7]. Amplitude of this polarization rotation depends on the efficiency of generation of the mediums anisotropy which is maximal when the modulation frequency Ω_m coincides with twice the Larmor frequency Ω_L, $\Omega_m = 2\Omega_L$.

A detailed theoretical treatment of nonlinear optical processes, especially NFE, presented in this section provides a good background for further discussions performed in this chapter.

3. Experimental Arrangements

The basic experimental arrangement for investigation of NFE is essentially the same as for all magneto-optical studies. It involves a light source, an appropriate sample, e.g. a vapor cell, and a detection system. In the studies of NFE the light comes from a tunable laser. For development and laboratory tests of the NFE magnetometers, their sensing samples (vapor cells) are subjected to well controlled magnetic fields produced by a coil system and protected from uncontrolled stray fields. The schematic of a typical setup in which modulated light is used is shown in Fig. 7.

In the following sections, we outline the most essential features of the principal elements of the NFE experimental setup.

3.1. Light Sources

Unlike in LFE, the NFE requires light that is sufficiently coherent and intense to create atomic Zeeman coherences. This means that laser sources are necessary for such experiments. The lasers need to be tunable and their frequency should be stabilized to the desired

---

[7]The "peanut" oriented at $0°$ is indistinguishable from the one oriented at $180°$ therefore the light-polarization is modulated at $2\omega_L$, rather than ω_L.
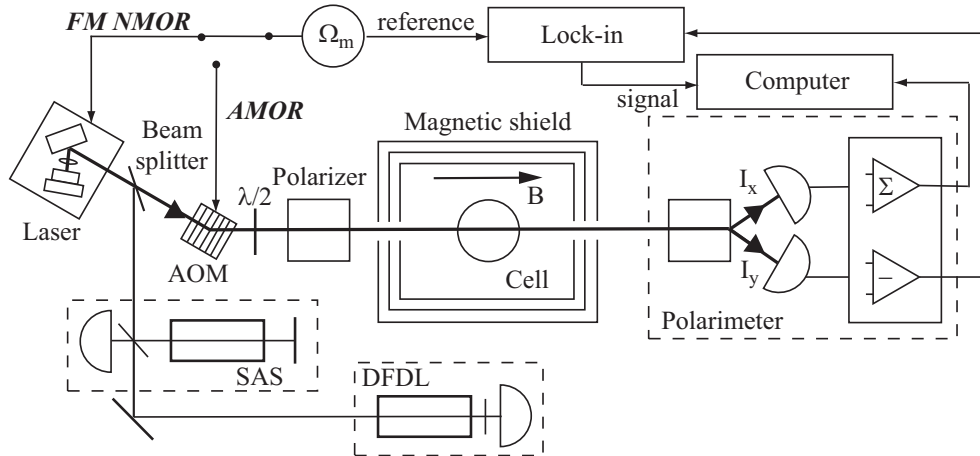
Figure 7. Typical setup for NFE experiments with modulated light. A laser light can be either frequency- or amplitude-modulated with a switch at the FM NMOR or AMOR position, respectively. The light of adjustable intensity traverses atomic vapors placed in the longitudinal magnetic field B. A multi-layer magnetic shield protects the atoms from external, uncontrollable magnetic fields. The polarization rotation is measured with a polarimeter and demodulated at a given harmonic of modulation frequency Ω_m. The signal is stored on a computer. SAS denotes saturated absorption frequency reference and DFDL the Doppler-free dichroic lock used for stabilizing laser frequency, $\lambda/2$ is a half-wave plate, and AOM the acousto-optical modulator. I_x and I_y are the intensities of the two orthogonally polarized outputs of the analyzing beam splitter. For balancing of the polarimeter the axis of polarizer prior the cell needs to be oriented at $45°$ relative to the x and y axes (see Sec. 3.4.).

atomic transitions. For example, in the setup shown in Fig. 7 the laser frequency is stabilized by a Doppler-free dichroic lock and additional frequency reference is provided by a saturated-absorption spectroscopy in an additional vapor cell. In the experiments where light modulation is used (FM NMOR or AMOR), the light frequency or intensity is varied[8]. Besides frequency control, laser sources for NFE may have rather modest parameters from the point of view of power and linewidth. Usually some mW output light power is sufficient, so inexpensive diode lasers are quite adequate. In more demanding applications external-cavity diode lasers may be applied with their frequency stabilized to atomic transition. For applications where power consumption and/or small size become is an issue, the vertical cavity surface emitting lasers (VCSELs) can be used.

3.2. Samples

In most of the existing applications, the NFE sensors are atomic gases contained in glass cells. Recently, novel materials were investigated for their possible use in quantum and nonlinear optics, like atoms inside hollow fibers [21, 22] and NV color centers in diamond crystals [23]. As outlined in Sec. 4.1., one crucial parameter for magnetometric applications

---

[8]In case of FM NMOR, the frequency of light is scanned around fixed light frequency.

that determines the device sensitivity is the linewidth of the resonance which is associated with the relaxation time of the coherences. Long relaxation times are also crucial for applications in quantum state engineering. Thus, it is essential that the sample possesses appropriate long-living states which can be affected by magnetic fields and connected by an easily accessible optical transition.

For ground-state coherence of atoms contained in a gas cell, the relaxation times is limited by several factors. One is caused by thermal movement of atoms and finite dimensions of the light beam probing the coherence. This is known as the transit relaxation. Usually, for typical cell temperatures and beam sizes, this effect limits the relaxation times to some μs which results in resonance widths of tens of kHz. Such linewidths do not allow very high magnetometric sensitivities, so various techniques are used to overcome the transit relaxation. One known technique is application of buffer, usually noble, gases. The atoms in a gas cell undergo elastic collisions with the buffer gas atoms which limit atomic free path and lengthen their interaction time with laser beams. At the same time, the elastic collisions do not substantially destroy the atomic coherences and, consequently, very narrow NFE resonances are obtained resulting in high magnetometric sensitivities. Another way of slowing down the relaxation is coating the internal cell walls with special anti-relaxation, most often made of paraffin, layer which protect atomic coherences from destruction during atom-wall collision. Thanks to such coating, an atom can survive about 1000 wall collisions before it decoheres/depolarizes [24, 25] and the coherence lifetime can be extended up to hundred of ms.

3.3. Magnetic Fields and Magnetic Shielding

Studying Faraday Effect requires good control over all magnetic fields acting upon the sample. The problem becomes particularly important with NFE, due to its high sensitivity to even very weak magnetic fields. Since the rotation of the polarization plane is determined by the magnitude of the field, its inhomogeneity within the cell leads to broadening and/or deformation of the NFE signals [26]. Moreover, the field orientation is also very important. Improper orientation reduces the rotation which causes systematic errors (heading errors) when measuring magnetic fields. Additionally, transverse components of the magnetic field mix the Zeeman sublevels which deteriorates Zeeman coherences and is very undesirable for applications in quantum-state engineering.

Familiar sources of homogenous magnetic fields are Helmholtz coils and solenoids. For studies of NFE in very low fields it is essential to reduce the effect of external fields, both the AC and the DC ones. While DC stray fields can be compensated by proper coils, the AC fields are most efficiently eliminated by shields made of appropriate ferromagnetic material of high permeability, e.g. mu-metal and ferrites. Well designed shields not only reduce the stray fields but, additionally, improve the homogeneity of the effective field acting on a sample. For example, by using the magnetostatic image method, it can be shown that the field generated by a current loop situated at $x = 0$ oriented parallel to the surface of the high permeability material placed at $x = a$, is the same as one produced by a pair of parallel loops separated by the distance $2a$. Thanks to that, the effective field produced by a coil in a magnetic shield is the same as from an infinite chain of coils. This fact may substantially improve homogeneity of the effective field acting upon the sample.

The choice of the shield material is of importance, too. The shields need to have possibly high magnetic permeability but they also must sustain the fields produced by the internal coils and not saturate. Besides that, the material should be free of fluctuations caused by random orientations of magnetic domains and thermal currents which could generate extra magnetic noise. For most demanding applications multilayered shields are designed with the most inner layer being made of ferrite and the others of other material such as mu-metal [27].

3.4. Detection of the Polarization Rotation

Measuring optical rotation requires sensitive polarimetric detection. While very different methods have been developed for various magneto-optical experiments, the detection technique most often employed for studies of NFE is based on balanced polarimetry.

The basic design of a balanced polarimeter consists of a polarizing beam splitter (e.g. Glan, Glan-Thompson, or Wollastone prism) which separates the analyzed beam transmitted by the sample into two orthogonally polarized beams, say along the x and y directions, and two identical photodetectors which measure the beam intensities (see Fig. 7). The whole system is oriented in such a way that for zero rotation the transmitted beam has its $\mathbf{E}$ vector at $45°$ with respect to the x and y axes, so the detectors record equal light intensities $I_x = I_0 \sin^2(\pi/4) = I_y = I_0 \cos^2(\pi/4)$. If, however, the light polarization rotates by the angle ϕ, the detectors record different light intensities $I_x = I_0 \sin^2(\pi/4 + \phi)$ and $I_y = I_0 \cos^2(\pi/4+\phi)$ which for small ϕ become $I_x \approx I_0(1+\phi)^2/2$ and $I_y \approx I_0(1-\phi)^2/2$. The difference of these signals, $I_x - I_y$, is then proportional to the rotation angle. When divided by doubled sum, $2(I_x + I_y)$, the difference signal becomes independent of the incident light intensity I_0 and yields directly the rotation angle. Moreover, fluctuations of I_0 in each detection channel cancel out and do not contribute directly to the noise of a rotation measurement. Such an arrangement is very useful for measuring small rotations with not-too-strong light intensities. For higher intensities, problems may occur since each detector is illuminated by a strong average intensity and resolving small intensity variations may be limited by the detector dynamic range and saturation.

The limitations caused by dynamic range of the detectors are less important for another detection technique which employs one detector only and where the sample is placed between two crossed polarizers. This method is known as the forward scattering [28]. The main advantage of the forward-scattering detection is its simplicity and elimination of a background which could deteriorate the signal-to-noise ratio and sensitivity: only the photons which contribute to the signal are detected for an ideal system. In a system with ideal polarizers, low optical thickness and no dichroism of the sample, optical rotation by angle ϕ yields the detector signal $I_0 \sin^2 \phi$ which for small angles is proportional to ϕ^2. In this way, a square of the rotation angle can be measured with high sensitivity but the signal does not allow one to determine the sign of the rotation angle. Such a homodyne detection is widely used in a Doppler-free polarization spectroscopy [29].

An interesting technique of measuring small rotations with very high sensitivity is based on homodyning the forward scattering signal with a coherent background. Such background is most easily obtained from non-scattered primary light beam by small uncrossing of the polarizers from their perfectly crossed position. If the uncrossing angle ε is small, but

still much bigger than the measured signal ϕ, $\phi \ll \varepsilon$, the detected intensity of a forward scattered light becomes $I = I_0 \sin^2(\varepsilon + \phi) \approx I_0(\varepsilon + \phi)^2 \approx I_0\varepsilon^2 + 2I_0\varepsilon\phi$. This signal consists of a constant background $I_0\varepsilon^2$ and a contribution proportional to ϕ. In this way, the sign of ϕ can be easily determined and the amplitude of the magneto-optical rotation is substantially increased by its homodyning with a coherent background which is responsible for multiplicative factor 2ε.

The heterodyne method can be modified to eliminate the constant background by modulating the coherent background and application of the phase-sensitive detection. In addition to the measured rotation ϕ this introduces a time dependent background $\varepsilon_0 \cos \Omega t$, where ε_0 is the amplitude and Ω the frequency of the introduced background. After demodulation of the resulting time-dependent light intensity, $I(t) = I_0 \sin^2(\varepsilon_0 \cos \Omega t + \phi) \approx I_0(\varepsilon_0 \cos \Omega t + \phi)^2$, only the $2\varepsilon_0\phi$ term is recorded with a high signal-to-noise ratio.

This simple discussion assumes optically thin samples with no dichroism and ideal quality polarizers. For more realistic cases with optically thick samples and imperfect polarizers corrections are necessary to the above expressions. The effect of dichroism, which introduces some elipticity of the transmitted light, may be taken into account thanks to different spectral responses of the dichroic and birefringent contributions. In particular, for a well resolved optical transition, the dichroic spectrum is characterized by asymmetric lineshape whereas the birefringence spectrum is symmetric with respect to optical transition frequency.

3.5. Electronic System

A standard signature of the Faraday effect, LFE or NFE, is the dependence of the angle of polarization rotation ϕ on the magnetic field B. It is represented by an asymmetric curve, centered at $B = 0$, such as the one shown in Fig. 8(a). Application of modulated light leads to the appearance of additional resonances at non-zero magnetic fields [Fig. 8(b)]. The positions of these extra (high-field) resonances are strictly determined by the light-modulation frequency through the relation

$$B = \frac{n_i\omega_m\hbar}{2g\mu_B},\tag{23}$$

where n_i is an integer. Application of modulated light for studying NFE was pioneered by Budker and co-workers who developed the technique of Nonlinear Magneto-Optical Rotation with Frequency-Modulated light (FM NMOR) [7]. In FM NMOR, frequency modulation of light resulted in modulation of the pumping rate of atoms. When modulation of the pumping light was synchronized with the precession of atomic polarization in a magnetic field (see Sec. 2.4.), the macroscopic, dynamic polarization of the medium is generated.

Frequency modulation of laser light can be realized particularly easily with diode lasers through modulation of the laser current. Current modulation, however, is not perfect as it is always associated with some amplitude modulation of the light emitted from the laser diode. Moreover, even pure frequency modulation may introduce light-shifts which have undesirable consequences, for instance, from a point of view of applications of NFE for magnetic-field measurements (systematic errors). On the other hand, the modulation of
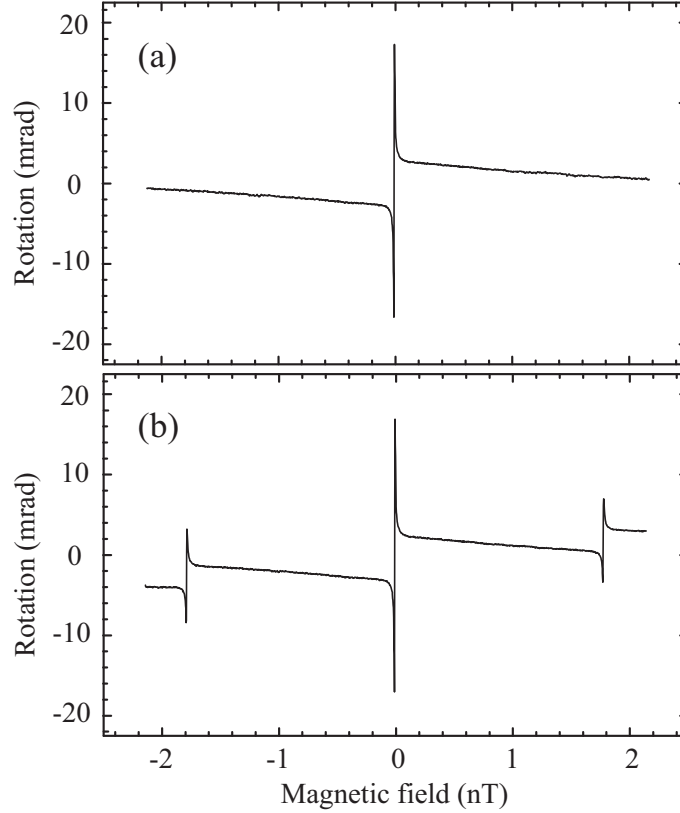
Figure 8. (a) Rotation of polarization plane vs. magnetic field observed with unmodulated light. (b) In-phase magneto-optical rotation vs. magnetic field recorded with amplitude modulated light ($\omega_m = 2\pi \times 25000$ 1/s).

the pumping rate by pure amplitude modulation of the laser intensity reduces the risk of light-shifts because the laser frequency may be made exactly resonant with the atomic transition. The NFE technique which relies on the modulation of laser intensity, known as Amplitude-Modulated Magneto-Optical Rotation (AMOR) has been introduced in Ref. [8]. An intrinsic advantage of AMOR technique is the ability to choose arbitrary modulation waveforms. In particular, in Ref. [8] it was shown that a square-pulse modulation of light intensity creates a comb of extra resonances occurring at multiplicities of $\omega_m \hbar / 2g\mu_B$. Pure amplitude modulation is most easily applied with the help of acousto-optical modulator (AOM).

FM NMOR and AMOR have much in common with the method of synchronous pumping already used in early optical-pumping experiments [30, 31].

NFE signals observed with the modulation techniques (FM NMOR and/or AMOR) are time-dependent and must be demodulated at a particular frequency. This is usually performed with the phase-sensitive (lock-in) detection which allows one to register both signals related to the modulation, the in-phase and quadrature signals, shifted respectively by 0° and 90° relative to the modulation signal.

An interesting alternative of a single-beam NFE arrangement is the two-beam setup, where one beam acts as a pump and the second, unmodulated beam as a probe [32]. This gives one the ability of optimization of NFE signals by varying pump- and probe-light intensities, detunings, and polarizations.

4.   Applications of Nonlinear Faraday Effect

In addition to the fact that NFE is a very interesting optical phenomenon on its own, it finds a number of interesting scientific and commercial applications. One group of applications is associated with ultra-high sensitive magnetometry. Magnetic-field measurements with such high sensitivity may be employed, for instance, in prospecting for natural resources or detecting distant magnetic objects, but also in testing of fundamental symmetries of nature. The other group of applications is the quantum-state engineering. In that case, NFE is exploited for controllable generation and modification of quantum states of the atomic system. Below the most important NFE applications are reviewed.

4.1.   Magnetometry

Applications of nonlinear magneto-optical phenomena for magnetic field measurements [33] have a long history. Since first experiments in the 1960s [34, 35], different configurations of optical magnetometers have been used. Recent interest in the field is driven by technological developments in opto-electronics, especially, the invention of small, tuneable, and inexpensive diode lasers. It enabled construction of various kinds of optical magnetometers with the sensitivity rivaling [6, 36, 37], or even exceeding [38] the sensitivity of magnetometers based on properties of superconductors (SQUIDs), long recognized as the most sensitive magnetometers. Currently, the demonstrated sensitivity of the most sensitive magnetometer, the, so-called SERF (spin-exchange relaxation-free magnetometer) [38], reached a level of a fraction of 10^{-15} T/$\sqrt{\text{Hz}}$ with its projected fundamental limit below 10^{-17} T/$\sqrt{\text{Hz}}$.

One fundamental challenge of contemporary magnetometry is miniaturization. Luckily, there are no principal constraints for making such devices small; accomplishments of opto-electronics and microfabrication of mechanical systems allow impressive reduction of the dimensions of optical magnetometers. Recently, optical magnetometers with volumes of a few mm^3 were demonstrated [39, 40]. These devices exploit microfabrication techniques for production of atomic vapor cells and optical elements for shaping and generation of light. Moreover, their low power consumption enables charging of the devices with batteries. The best micromagnetometers reach a magnetic-field measurement sensitivity below 7×10^{-14} T/$\sqrt{\text{Hz}}$ [41]. Exciting miniaturization possibilities are also opened by novel photonic materials, the diamonds with NV-color centers [42–44].

4.1.1.   Characteristics of Optical Magnetometers

One of the most important characteristics of any magnetometer is its sensitivity. For all optical magnetometers, and hence for NFE magnetometers, quantum mechanics sets a fundamental limit on the magnetic-field-measurement sensitivity. This limit is associated with

fluctuations in the numbers of atoms[9] and photons that contribute to the measured optical signal. Since the number of contributing atoms N is described with the Poisson statistics, fluctuations in atomic number is given by $\sqrt{N}$. Thus the fundamental sensitivity limit due to the atomic shot-noise is given by

$$\delta B_{at} = \frac{\hbar}{g\mu_B}\sqrt{\frac{1}{NT\tau}}, \tag{24}$$

where $T = 1/\gamma$ is the coherence lifetime and τ is the time of the performed measurement[10].

Another contribution to the sensitivity limit is associated with fluctuations in the number of detected photons N_{ph}. If the measured quantity is the rotation of polarization, as it is for NFE magnetometers, the shot-noise limit on that measurement is given by

$$\delta\phi_{ph} = \frac{1}{2\sqrt{N_{ph}\tau}}, \tag{25}$$

which corresponds to the limit on the magnetic-field-measurement sensitivity

$$\delta B_{ph} = \frac{\hbar}{g\mu_B}\frac{\gamma}{\phi_N}\frac{1}{2\sqrt{N_{ph}\tau}}, \tag{26}$$

where ϕ_N is the NFE signal amplitude.

Since fluctuations in the number of atoms and photons are uncorrelated, these noises add in quadrature determining the fundamental quantum limit on the sensitivity

$$\delta B_{ql} = \sqrt{\delta B_{at}^2 + \delta B_{ph}^2}. \tag{27}$$

Depending on particular experimental realization, either atomic or photon shot-noise may dominate. However, in an optimized magnetometer both noises are comparable [45] which gives $\delta B_{ql} = \sqrt{2}\delta B_{at}$.

Very often magnetometers suffer from different kinds of magnetic noise that limit ultra-precise measurements of the field. A remedy for such strong noise is the, so-called, gradiometer mode. In this mode, the magnetic field is measured by two spatially separated magnetometers whose independent readouts are subtracted. In that way, the inhomogeneous magnetic field generated by a local source can be precisely measured whereas the magnetic field background common for both magnetometers may be eliminated. The gradiometer arrangements find many applications (see, for example, Secs. 4.3. and 4.4.).

An important characteristic of a magnetometer is its dynamic range. In the NFE magnetometers with CW excitation, the dynamic range of the magnetic-field measurements ΔB is limited by the width of the recorded resonance, $\Delta B \approx \hbar\gamma/g\mu_B$. While for $B < |\Delta B|$ there is an unambiguous relation between the rotation angle and the magnetic field, for

---

[9]In fact, the limit on the sensitivity is set by the uncertainty in determination of projections of total angular momenta of atoms. Since projections of the total angular momentum are noncommuting operators, $[F_x, Fy] = iF_z$, where F_i is the total angular momentum projection on i direction, thus the spin projection-noise arises due to $\delta F_x \delta F_y \geq |F_z|/2$.

[10]Please note that some parameters on the order of unity, such as the total value of angular momentum, were omitted in Eq. (24).

the stronger fields, $|B| > \Delta B$, the same magneto-optical rotation corresponds to two different values of the field, and for even stronger fields $|B| \gg \Delta B$ there is no rotation [see Fig. 8(a)]. The relaxation rate γ determines thus the sensitivity, as well as the dynamic range of the magnetometer; the narrower the resonance, the higher the sensitivity but smaller the dynamic range of the magnetometer. In order to achieve the magnetometer of the desired sensitivity and dynamic range, the width of the resonance needs to be adjusted. It can be done, for example, by varying the resonance width by adjusting light intensity and power broadening of the resonance.

In order to alleviate the limitations on the small dynamic range of the magnetic-field measurements, modulation techniques were employed (see Sec. 2.). It enables expanding of the NFE magnetometers dynamic range to the Earth magnetic field, which is very important in numerous applications because it eliminates necessity of shielding or compensating external, uncontrollable magnetic fields.

Another relevant parameter of optical magnetometers is its bandwidth which reflects magnetometer response time to a change of a measured magnetic field. Although the Larmor precession has no inertia and atoms instantaneously react to the field change, it takes a finite time to measure the difference in the recorded signal. It can be shown that the response of a CW (low-field) magnetometer can be modeled as that of a low-pass filter and hence the natural magnetometer bandwidth is equal to $1/2\pi T$ [46]. The bandwidth of a magnetometer can be increased by amplifying its output signal but this also affects the output noise of the magnetometer [47]. Thus, the increase of the magnetometer bandwidth is usually at the price of reduction of the signal-to-noise ratio.

The same relation for the bandwidths that holds for the CW magnetometers also works for the NFE magnetometers with modulated light; the bandwidth of these magnetometers is also determined by the NFE resonance width. It is noteworthy, however, that for the magnetic-field measurements with phase-sensitive detection, more stringent limitation on the bandwidth may appear. In such a case, the bandwidth of the magnetometer may be determined by the time constant τ_c of the lock-in in which case the bandwidth is given by $1/2\pi\tau_c$,

Other important characteristic of a magnetometer is whether it enables measurements of static and quasi-static fields or it allows fast-oscillating magnetic fields to be detected. Although most optical magnetometers are used for measuring DC fields, there is a class of devices that can be employed for measuring AC magnetic fields [48, 49]. The significant advantage of the AC optical magnetometers is their tuneability for measurements of the fields oscillating at specific frequencies. Application of a bias field allows one to shift the magnetometer resonance frequency and in such a way detect selectively the field at the desired frequency. The measurements of the oscillating fields up to 100 kHz were already demonstrated and there are no physical limitations preventing significant expansion of the magnetometer frequency range.

An important feature of a magnetometer is whether it enables a measurement of field magnitude only (scalar magnetometer) or if it also provides information about the field direction (vector magnetometer). Most optical magnetometers, including the NFE-based devices, are scalar. An advantage of such magnetometers is their insensitivity to the field orientation, in particular, heading errors, which may be important for devices operating at moving platforms. Nevertheless, there are standard techniques that enable transformation

of scalar magnetometers into the vector ones by application of small oscillating fields in three orthogonal directions [50, 51]. Since small fields along with, and transverse to, the measured magnetic field contribute differently to the magnetometer readout, modulation of the total field in all three orthogonal directions with various frequencies and successive demodulation of the detected signal at these frequencies enables extraction of the information about the direction of the measured field. An alternative method, exploited in the optical magnetometers, is observation of amplitudes of two resonances detected at given multiplicities of the Larmor frequency which vary with a direction of light propagation with respect to the magnetic field [52, 53]. The ratio of these amplitudes can be evaluated from simple analytical formula. It is insensitive to the measured field magnitude but does depend on the field orientation. This provides a convenient way of measuring the field direction. The method enabled reaching angular sensitivity of 4×10^{-3} degree/$\sqrt{\text{Hz}}$ [52].

4.1.2. Low-magnetic Field Measurements

Applicability of NFE with CW light for measuring magnetic fields was first suggested in Ref. [5]. Yet, it was only in Ref. [45] when the first detailed studies of this magnetometric technique was experimentally analyzed. The authors of Ref. [45] observed NFE with rubidium vapor contained in an anti-relaxation-coated buffer-gas-free cell. Analysis of the polarization rotation versus different physical parameters yielded optimal conditions for the observation of NFE. The recorded signals were 10 mrad in amplitudes and had widths of 100 pT. By taking advantage of such narrow resonances, magnetic-field measurements with a sensitivity of 4×10^{-16} T/$\sqrt{\text{Hz}}$ were demonstrated. This sensitivity is comparable with the sensitivity of SQUIDs. Therefore, in many applications NFE magnetometers can replace superconductive devices, eliminating the problem with a necessity of cryogenic cooling. The intrinsic drawback of such NFE magnetometers is their limitation for detection of low fields only. In particular, the dynamic range of the device described in Ref. [45] was ± 100 pT. Measurements of such fields demand passive and/or active shielding of external, uncontrollable magnetic fields which usually are orders of magnitude stronger than the detected field.

4.1.3. High-magnetic Field Measurements

As already noted above, the limitation of NFE magnetometers for detection of weak fields was only successfully relaxed by application of a frequency- [7] and amplitude-modulated [8] light. As shown in Sec. 2.4., the modulation of light leads to the appearance of strong magneto-optical resonances, whose positions vs. magnetic field are strictly determined by the modulation frequency. The high-field resonances have amplitudes and widths not unlike zero-field resonances (see Fig. 8), thus the sensitivity of stronger-field measurements is comparable with the ones achieved for the zero-field measurements (see Sec. 4.1.2.). Reaching higher fields eliminates necessity of shielding or compensating external, uncontrollable magnetic fields.

High-field NFE magnetometers operate in either passive or self-oscillating mode. In the passive mode, an external oscillator modulates the light while the rotation of the light polarization is measured at a given harmonic of the modulation frequency. Figure 8(b)
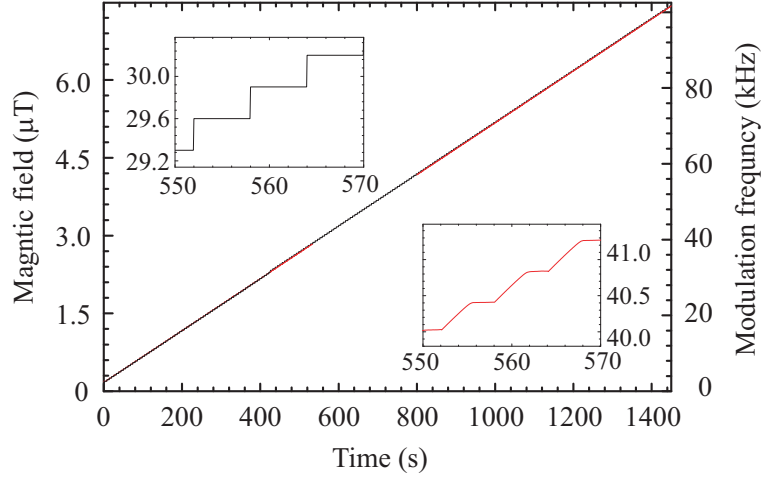
Figure 9. Magnetic-field tracking with the NFE magnetometer operating in the passive mode. Every 9 s, the total magnetic field was increased by 15 nT and the modulation frequency was subsequently adjusted with the feedback system such that the condition for the effective of the higher-field resonance was fulfilled.

demonstrates that a given modulation frequency and magnetic field correspond to a particular high-field NFE resonance. Thus, each change of the field magnitude causes a modification of the measured NFE signal. In the passive-mode magnetometers, one may track the magnetic field by keeping a fixed value of the signal, $\phi = $ const. It can be done, for example, by continuous fulfilling the condition for effective generation of the high-field resonance, for instance, $\omega_m = 2\Omega_L = 2g\mu_B/\hbar B$, for which the amplitude of the polarization rotation is maximal; the field change is followed by such an adjustment of the modulation frequency Ω_m in a feedback loop that NFE signal is maximal.

A significant advantage of the passive-mode magnetometers is their insensitivity to various types of noise. Application of the phase-sensitive detection strongly suppresses the noise at frequencies other than the reference frequency. For instance, one can reduce the 50-Hz or 60-Hz noise associated with AC lines. The drawback of the mode, however, is the magnetometer low bandwidth related to a finite time constant of a lock-in amplifiers. Therefore, the best application of passive-mode magnetometers is for detection of static or slowly varying magnetic fields.

In Fig. 9 the magnetic-field tracking signal obtained with the passive-mode NFE magnetometer employing amplitude-modulated light is shown [54]. Every 9 s, the magnetic field was increased by 15 nT and the modulation frequency was adjusted according to the scheme described above. Determining a new value ot the magnetic-field magnitude usually took 2-3 s, which depended on the field-change magnitude, the lock-in time constant, etc. While maintaining a sensitivity of 4.3×10^{-13} T/$\sqrt{\text{Hz}}$, the device was able to track magnetic fields in a range of a few μT. Moreover, in Ref. [54], extension of the dynamic range toward Earth magnetic field and further increase of the device's sensitivity were predicted.

In general, the self-oscillation mode of optical magnetometers, is based on using the

detected optical signal for modulation of optical [34, 55, 56] or RF excitation [34, 57] of atoms. Since the signal oscillates at the Larmor frequency or its harmonic, in such an arrangement the condition for the efficient generation of the higher-field magneto-optical resonances is automatically fulfilled. When the detected signal is amplified sufficiently, the oscillation builds up spontaneously (seeded by noise) at the resonant frequency. Due to no inertia in precession of spins, a change of the magnetic field is immediately reflected in the frequency of oscillations of the optical signal and hence the light modulation frequency.

Operation of NFE magnetometers in the self-oscillating mode is achieved by feeding amplified and phase shifted non-demodulated, time-dependent NFE signal directly to the light modulation controller, e.g., AOM driver [55,56]. The signal is phase shifted such that a 90° phase shift between the polarization rotation and the modulation frequency is achieved. While broad bandwidth is a big advantage of the self-oscillation mode, its drawback is lower sensitivity than sensitivity of the passive-mode magnetometers. Since no filters are applied to the signal, whole-spectrum noise contributes to the measured signal reducing signal-to-noise ratio. Despite the fact that the atoms themselves work as a narrow-band filter selectively transmitting only frequency $2\Omega_L$, the additional noise may introduce frequency jitter and distort measurements of magnetic fields.

A typical self-oscillation signal reported in Ref. [55] is shown in Fig. 10. For the purpose of a wide bandwidth demonstration, the NFE signal was heterodyned with a fixed reference with a time constant of 50 μs. The tracking of the field step is quasi-instantaneous,
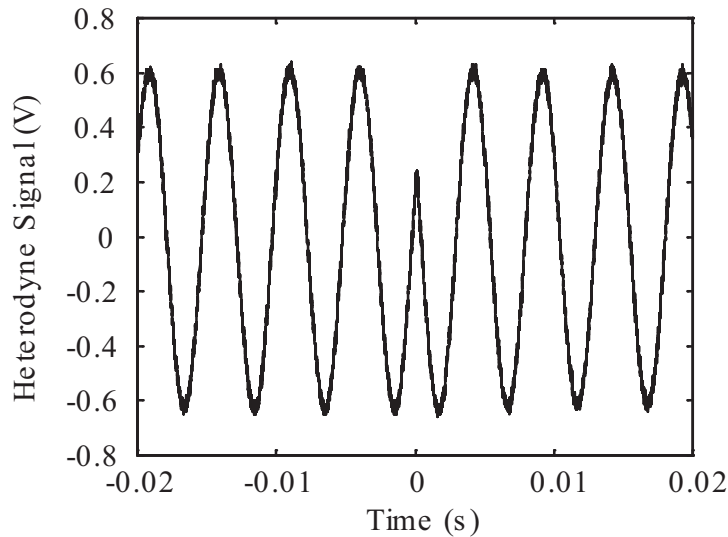

Figure 10. Time-dependent rotation of the light polarization observed with NFE magnetometer in the self-oscillating mode. In order to demonstrate high speed of the magnetometer the signal was heterodyned with the reference signal. At $t = 0$ a sudden change of 25 nT of the total magnetic field, resulting in a jump of the oscillation phase, was applied. The bandwidth of this magnetometer was above 1 kHz. From Ref. [55].

without apparent overshoot or ringing; the sudden change of about 25 nT applied to the bias

field at $t = 0$ results in a phase-jump in the heterodyne signal. The demonstrated bandwidth of the magnetometer exceeded 1 kHz with a sensitivity of 300 fT for a measurement time of 1 s.

In Sec. 4.1., several schemes of NFE magnetometers were discussed. They differ in sensitivity, dynamic range, bandwidth, etc., hence each of them has own its advantages and disadvantages; while passive-mode magnetometers seem to be better for measuring static or quasi-static magnetic fields, self-oscillating magnetometers can be used for measuring varying fields.

4.2.   Nuclear Magnetic Resonance

The first practical application of NFE magnetometers to detect the nuclear magnetic resonance (NMR) was described in Ref. [10]. For that purpose the used an NFE magnetometer with frequency-modulated light.

NMR is a powerful technique exploited in studies of structure and dynamics on micro- and macroscopic scale and its applications range from medicine to real-time process control [58]. A good example of the element extensively employed in NMR is ^{129}Xe. Its advantages include the polarization via spin-exchange collisions, strong chemical shifts, which makes it a good probe to study physicochemical environment, and long relaxation times.

For the NMR measurements, a typical NFE experimental apparatus such as one described in Sec. 3., was modified. In addition to the standard setup elements like laser, magnetic shield, vapor cell, etc., a solenoid piercing the shield was mounted in the vicinity of the vapor cell. The solenoid was longer than the shields thus magnetic field lines associated with the solenoid were closed outside the shield. It enabled generation of a homogenous magnetic field of about 50 μT inside the solenoid and almost no field in other parts of the shield, particularly, within the vapor cell (suppression factor on the order of 10^5). The solenoid field was necessary to orient the polarization of the Xe sample introduced into the shield via the solenoid. The 1.7 cm^3 sample containing natural abundance xenon at 3.7 torr pressure, spin-polarized (1% polarization) by spin-exchange collisions with optically pumped atoms outside the shield. A magnetic field of 14 nT perpendicular to the solenoid axis was generated inside the shield with a set of magnetic-field coils. In such a way, the detector measured a net magnetic field, that is, the field from the coils and polarized Xe but not from the solenoid. The application of that field enabled shifting of the NFE resonance position towards higher fields leading to significant reduction of the $1/f$ noise and a possibility of using the light-modulation technique for tracking of the samples demagnetization. The magnetometer worked in the passive mode (Sec 4.1.3.).

In Fig. 11 a typical data of Xe magnetization decay vs. time is shown. Each point was measured for about 3 s which enabled achieving S/N ratio at a level of 10. According to the authors, the S/N ratio could be improved by at least 2 orders of magnitude by better geometry of the experiment. In the performed experiment, the magnetic field generated within the vapor cell by polarized Xe was roughly 5000 times smaller then the one inside the sample.

In order to distinguish magnetic-field changes resulting from the decay of the Xe polarization from slow drifts of the other fields, for instance, related to the instability of current sources used for the magnetic-field generation, thermal current flowing in the shield, etc.,
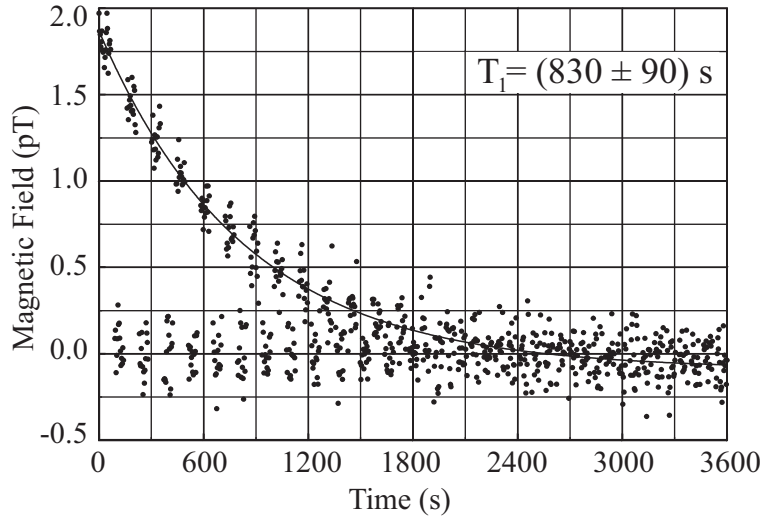
Figure 11. Xe-magnetization signal recorded with the NFE magnetometer [10]. The upper trace was generated by polarized Xe, while the lower trace is the reference enabling to eliminate the effect of slow drifts of the magnetic field. The traces were obtained by moving the xenon sample into and out of the shield in 1-minute intervals.

differential measurements were performed. In that case, the Xe sample was mechanically moved in and out of the shield which modulates magnetometer readout.

As seen in Fig. 11, an exponential decay of the Xe polarization from ≈ 2 pT to 0 with a relaxation rate of $(7.6 \pm 0.87) \times 10^{-3}$ 1/s was measured.

4.3. Magnetic Particle Detection

Another interesting application of NFE magnetometers is detection of magnetic particles. Such particles are micro- or nano-objects made of ferro- or paramagnetics. When bonded to other physical objects or chemical compounds, these particles can selectively react with given types of materials and/or chemicals which enables detection of such material/substances at very low concentrations. This technique is commonly used in medicine and biosciences, e.g., for DNA-targeting. Moreover, application of external fields is a convenient way of manipulation of the magnetic particles, as well as bonded objects. The particles are also broadly used as contrast agents in NMR.

In order to characterize magnetic particles and hence monitor behavior of tagged objects, ultra-precise measurements of magnetic fields are needed. Such devices as SQUIDs [59] and giant magnetoresistive (GMR) sensors [60,61] were used for this sake. Each of the techniques has its advantages and drawbacks; SQUIDs have very high sensitivity but they require cryogenic cooling, while GMR sensors can be extremely small (on the order of μm) but the measured sample needs to be bring extremely close to the sensor. The NFE magnetometers reach sensitivity comparable to SQUIDs and do not require cryogenic cooling, hence they seem to be ideally suited for the magnetic-particle detection.

The first demonstration of the magnetic-particle detection with the NFE magnetometers

was described in Ref. [9]. The layout of an experimental arrangement is shown in Fig. 12. An important modification of an experimental apparatus with respect to setups tradition-
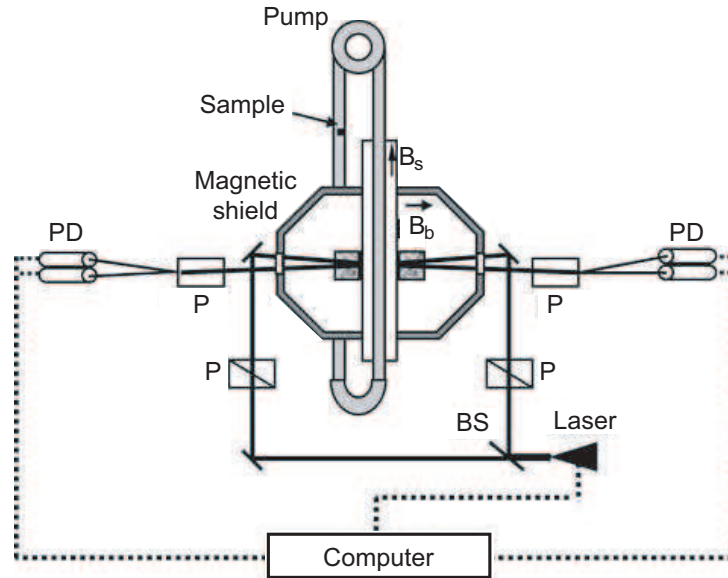

Figure 12. Experimental setup used for the magnetic particle detection. The magnetometer was operated in the gradiometer mode, i.e., the field was measured by two spatially separated magnetic-field sensors, which enabled detection of the magnetization of the magnetic particles flowing through the shield. The orientation of the particles' magnetization was assured with the piercing solenoid generating a field of $B_s = 50$ μT. The smaller bias field $B_b = 70$ pT applied perpendicularly to the solenoid enabled detection of the magnetization using the passive-mode NFE magnetometers. P stands for the polarizers, PD for the photodiodes, and BS for the beam splitter. From Ref. [9].

ally used in NFE measurements (see Fig. 7) was, in addition to the piercing solenoid (see Sec. 4.2.), an application of two vapor cells enabling gradiometric measurements (Sec. 4.1.). The 1-cm^3 cells were placed symmetrically with respect to the solenoid in a distance of 1.5 cm. The monitored particles within the solenoid were spin-oriented by $B_s = 50$ μT field. When there were no particles within the solenoid, the gradiometer cells were subjected only to a bias field of $B_b = 70$ pT, perpendicular to the solenoid axis, yielding zero differential signal. Introduction of the particles into the solenoid resulted in a field change in each cell; in one cell the sample magnetization B_e added up to and in the other subtracted from the bias field which results in non-zero gradiometer signal. That arrangement allowed a sensitivity of 100 fT/$\sqrt{\text{Hz}}$ to be achieved [11].

In Ref. [9], the study of three types of magnetic particles: multi- and single-domain cobalt particles of 150 μm diameter, 1 μm superparamagnetic magnetite particles, and ferro-

---

[11]For more details on magnetometer apparatus see Ref. [62].

magnetic cobalt nanoparticles of 120 kA/m magnetization were described. All the particles were suspended in water circulating through the solenoid within the shields. An example of the results obtained with the cobalt multi-domain particle is shown in Fig. 13. Each time
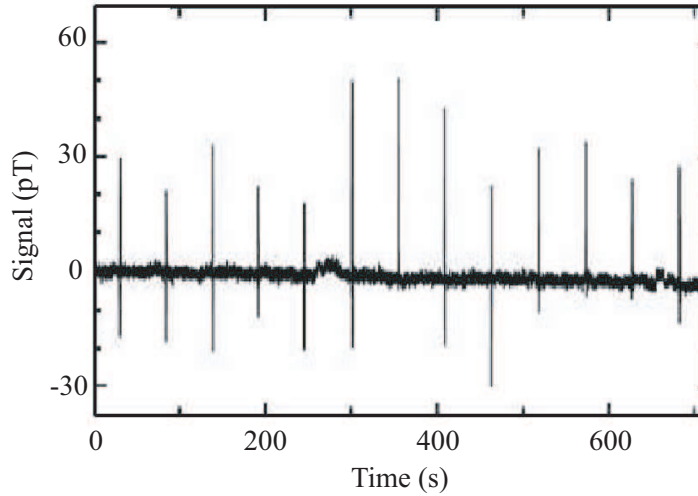

Figure 13. Magnetic detection of the cobalt multi-domain particle suspended in water flowing through the shield with a flowing rate 30 ml/min. Each time the particle traverses the magnetometers the strong gradiometer signal was recorded. The scattering in the amplitude of the signal was due to different positions of the particle inside the water tube each time it flew in vicinity of vapor cells. From Ref. [9].

the particle passed the gradiometer, the spike-like signal was observed. The amplitude of the signal depended on the magnetic field generated by the particle, as well as the water-flow rate, i.e., the time that the particle spent in a vicinity of the cells. Fluctuations in the amplitudes of the signal originated from the spread of particle's positions while traversing between the cells. Estimates performed in Ref. [62] showed that the detection limit on a size of the cobalt particle is about 20 μm for a multi-domain particle and about 5 μm for a single-domain particle.

Very interesting results were obtained for detection of amin-coated magnetite super-paramagnetic particles of about 1 μm. Such particles are used for tagging, capturing, and extracting DNA from living organisms [63]. The authors of Ref. [9] proved the possibility of real-time detection of a sample containing 4.5×10^5 particles and of 5×10^3 particles with averaging.

Exciting alternative for the discussed applications may be a use of millimeter-scale cells [64]. Application of these cells would enable bringing a sample closer to the magnetic-field sensor which would enhance the detection sensitivity. This possibility, however, has not been yet experimentally verified.

4.4. Magnetic Resonance Imaging

Very appealing application of NFE magnetometers and a natural extension of the previously described applications is magnetic resonance imaging (MRI). MRI is a method enabling extraction of unique information on spatial distribution of specific chemicals within a sample. It is widely used in medicine, material science, geology, etc. Traditionally, MRI is based on detection of a change in the magnetic flux generated by nuclear spins precessing in an external magnetic field. It is routinely realized with induction pick-up coils. While very simple, this technique suffers strongly from the $1/f$ noise which implies use of higher precession frequencies corresponding to very strong magnetic field (above 1 T). This is a serious obstacle, especially taking into account a required field homogeneity at the ppm level. Such fields are generated by specially prepared solid or superconductive magnets which limits MRI applications to relatively small, nonmagnetic samples only, reduces mobility and makes standard MRI devices very expensive. Therefore, development of the low-field MRI technique is very much desired.

In order to realize MRI at low magnetic fields, a sensitive technique of magnetic-field detection needs to be used. One solution is application of SQUIDs [65] which enable reaching much higher sensitivities than standard pick-up-coil technique. Since they require cryogenic cooling and complex electronics for multi-channel detection their application also in this case is limited. Alternative technique exploits NFE magnetometers [11]. Unlike other MRI techniques, it is based on detection of DC rather than AC magnetic fields. It is done in the, so-called, remote-detection arrangement, in which information about an analyte is transferred onto a mobile spin-polarized substance, and is successively read out at a different location [66, 67]. The signal detected by the NFE magnetometer is the net, longitudinal magnetization of the spin-polarized sample. An important advantage of the remote detection scheme is an ability of independent optimization of conditions for encoding and detection regions and continuous measurements of MRI signals.

The experimental setup used for MRI in Ref. [11] was very similar to the one shown in Fig. 12 and discussed in Sec. 4.3.. The most important difference in comparison to two previous measurements was introduction of the prepolarization and encoding regions in the water-flow system. The water was prepolarized by a 0.3 T magnet situated a couple of meters away from the shield. The polarized water flew into the encoding region where it interacted with an encoding field of 3.1 mT and a sequence of magnetic-fields pulses. The first pulse of the sequence, the $\pi/2$ pulse, rotated the spins to a plane perpendicular to the encoding magnetic field, which resulted in their precession. Successively, a pair of orthogonal magnetic-field-gradient pulses was applied. Different precession frequencies corresponding to different geometrical positions allowed to store the spatial information in the phases of spins' rotation. After the application of a second $\pi/2$, the phase-encoded spatial information was stored in longitudinal magnetization of the sample. Phase-encoded water was then transferred into the magnetic shield via the piercing solenoid. Introduction of the water changed magnetic fields in both cells and hence readouts of the whole magnetometer.

An example of the MRI results obtained with the NFE magnetometer and a phantom consisting of two parallel cylindrical channels is shown in Fig. 14. The images were obtained by cycling phase of the second $\pi/2$ pulse, modifying gradient amplitudes along the encoding directions, and performing Fourier analysis of the signal. That procedure yielded
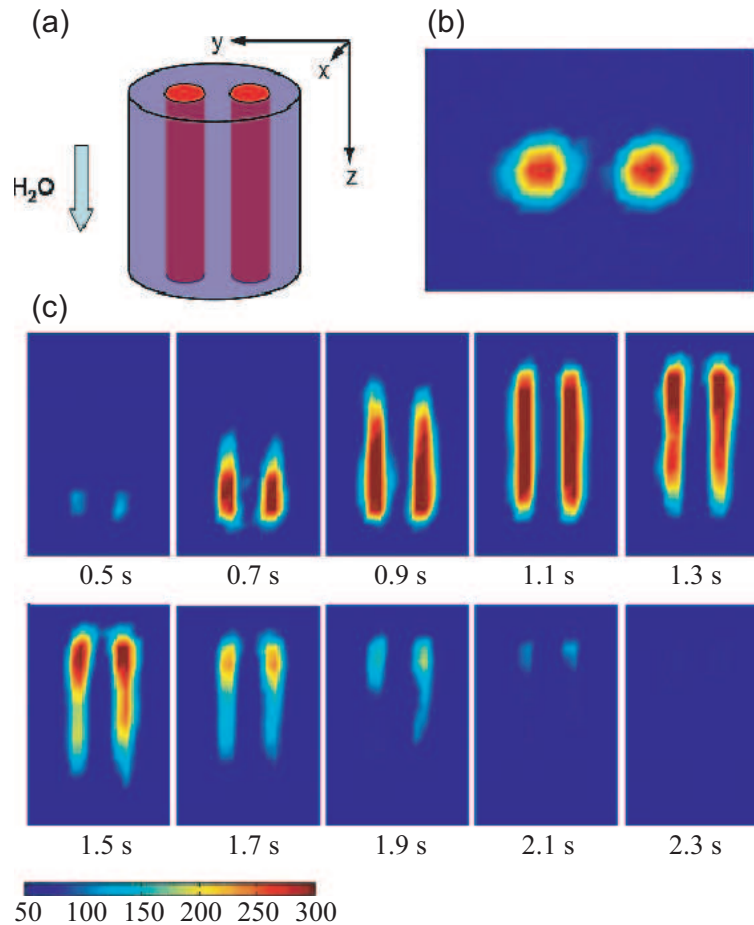
Figure 14. Magnetic resonance images obtained with the NFE magnetometer. (a) Phantom consisting of two channels of 3.2 mm in diameter and 25 mm length separated by 5.1 mm. (b) Image of the cross-section of the encoding volume in the xy-plane, perpendicular to the flow direction at $t = 1.1$ s. (c) Time-resolved images in the yz-plane, parallel to the flow (yz). From Ref. [11].

a spatial resolution of 1.6 mm perpendicular and 4.5 mm parallel to the encoding field and a temporal resolution of 0.1 s. In the experiment, the resolution was determined by the relaxation rate of the water polarization. The authors of Ref. [11] expected improvement of the resolution by shortening of water travel time from the prepolarization to the detection regions and/or by application of a stronger prepolarizing magnet.

Reference [11] demonstrated large potential of NFE magnetometers for MRI applications. Advantages of the technique are its high sensitivity, good spatial and temporal resolutions, and, most importantly, application of weak magnetic fields. Low fields eliminate problems associated with the field generation, appearance of magnetic-field artifacts, limitation of the technique for studying the nonmagnetic samples only, lack of the MRI device mobility, etc. These features are the reason for which the application of the NFE

magnetometry for MRI gain increasing attention.

4.5.   Selective Addressing of Atomic Coherences

In addition to the applications described above there is a rapid development of the NFE methodology for quantum-state engineering. This is caused by the fact that the same quantum superpositions which are responsible for the nonlinearity in the Faraday effect are also fundamental for storage of quantum information in atoms and quantum-state engineering. In particular, the techniques of slowing down coherence relaxation by paraffin-coating of cell walls or introduction of a buffer gas is the most effective way of extending the qubit lifetime. Moreover, the studies of NFE revealed that appropriate choice of modulation frequency with respect to the Larmor frequency enables selective generation of the atomic coherences between specific Zeeman sublevels of a given atomic state and successive modification of the state [32, 68, 69]. Since these coherences determine material properties, control over their creation and evolution allows one to generate media possessing unique physical, in particular, optical properties.

In Fig. 15 visualized density matrices containing different-order coherences, i.e., coherences between states with different values of the magnetic number m, are shown. As seen
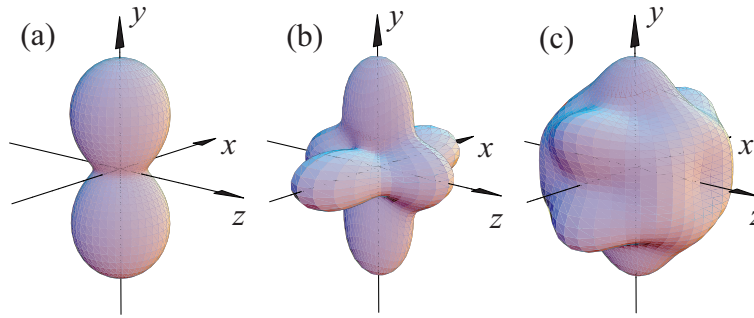

Figure 15. Visualized density matrices describing atomic systems with coherences of different orders: $\Delta m = 2$ (a), $\Delta m = 4$ (b), and $\Delta m = 6$ (c). The plots are drawn for the $F = 3$ state. From Ref. [32].

in Fig. 15(a), the $\Delta m = 2$ coherences correspond to the two-fold symmetric structure discussed above. Similarly, the $\Delta m = 4$ and $\Delta m = 6$ coherences are represented by the four- [Fig. 15(a)] and six-fold [Fig. 15(c)] symmetric shapes, respectively. In general, the symmetry of the visualized density matrix reflects an order of the coherences that exist in the atomic medium. Exploiting these symmetries enables generation of specific coherences. It was discussed in Sec. 2. that deviation from the sphericity of the visualized density matrix is a signature of an optical anisotropy of the medium. Thus, precessions of any of the shapes shown in Fig. 15, for example, in the external magnetic field, leads to the modulation of the probe-light polarization at different frequencies: $2\Omega_L$, $4\Omega_L$, or $6\Omega_L$. Demodulation of the NFE signal at these frequencies allows one to selectively detect the coherences of a given order.

The NFE signal with the resonances associated with the coherences of different orders are shown in Fig. 16 [32]. The resonance observed at twice the Larmor frequency
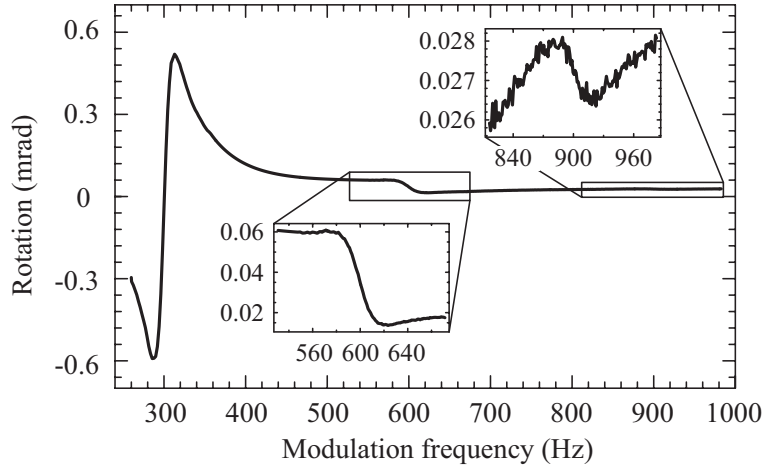

Figure 16. NFE signal recorded with frequency modulated light. The resonances at 300 Hz, 600 Hz, and 900 Hz are associated with $\Delta m = 2$, $\Delta m = 4$, and $\Delta m = 6$ coherences existing in atoms. From Ref. [32].

($\Omega_m = 2\Omega_L \approx 2\pi \times 300$ 1/s) is related to the $\Delta m = 2$ coherences ($\Omega_L \approx 2\pi \times 150$ 1/s). Similarly, the resonances at four ($\Omega_m \approx 2\pi \times 600$ 1/s) and six times ($\Omega_m \approx 2\pi \times 900$ 1/s) the Larmor frequency correspond to the $\Delta m = 4$ and $\Delta m = 6$ coherences, respectively. It was verified that all these resonances have different light-intensity dependences which indicates that different numbers of photons are needed for their generation and detection. In particular, the resonances associated with the higher-order coherences have significantly smaller amplitudes than those related to the lower-order coherences. This is expected since a photon is a spin-one particle and it can only generate coherences of $\Delta m \leq 2$. Generation of the higher-order coherences requires involvement of more photons which usually is less efficient than a single-photon interaction, thus the amplitudes of the NFE resonances associated with these coherences are smaller.

From a point of view of quantum-state engineering a better control over efficiency of coherence, especially the higher-order coherence, generation is needed. Therefore, a new, NFE based technique was elaborated [69]. With this technique, the higher-order coherences are generated in a multi-step process. In such a process, $\Delta m = 2$ coherence is first generated, and then the coherence is "updated" to $\Delta m = 4$ coherence by interaction with another photon. In order to selectively generate the $\Delta m = 4$ coherences, the second photon needs to be appropriately polarized with respect to the first photon; the two photons needs to have orthogonally polarized. Application of two orthogonally polarized photons allows the $\Delta m = 4$ coherences to be generated simultaneously causing destruction of the $\Delta m = 2$ coherences. As demonstrated in Ref. [69], the efficiency of higher-order coherence generation was significantly increased, which gave better control over creation of the multi-level quantum state was achieved.

Important feature of the described techniques is a possibility of coherence transfer be-

tween different atomic states. This was demonstrated in Ref. [32] by tuning the pump and probe light to two different hyperfine transitions of rubidium. In such a case, the pump light generated the coherences in the ground state which were successively excited to the upper atomic state. Since the excite state lifetime is 30 ns, the atoms instantaneously relax to one of the hyperfine ground states. The ones that relaxed to the same ground state from which they were excited can further interact with the light. However, those that decay to the other state do not interact with the pump light. Existence of the coherences in the latter state is reflected in modulation of the probe light. The modulation of the probe light tuned to the different than pump ground state, reported in Ref. [32], proved a possibility of transferring Zeeman coherence between different atomic states.

NFE provides an effective way of manipulation of atomic quantum states. The states can be engineered, i.e., the coherences may be selectively generated and the generated quantum state may be controllably modified. It should thus be possible to employ this technique in quantum computations for physical realization of multi-dimensional quantum "bits". Such multi-dimensional "qubits" would allow one to store more information than it is possible with "traditional" qubits. Simultaneous realization of the multidimensional "qubits" within the same atomic structure reduces one of the most severe limitations of quantum computations related to the exponential increase of the decoherence rate of a system of interacting qubits with an increase of its size. With the described technique the lifetime of the multi-dimensional "qubits" reaches tens of ms.

5.   Conclusions

This chapter reviewed techniques and mechanisms related to nonlinear Faraday effect and presented some of its most important applications. We had discussed theoretical foundations of the phenomenon focusing on the relation between nonlinearity of the effect and the light-induced atomic coherences. Much attention was drawn to the modulation techniques (FM NMOR and AMOR) which substantially increase the range of possible applications. After describing the most essential experimental aspects, several specific applications were discussed: magnetometry, NMR, MRI and magnetic particle detection, as well as quantum state engineering.

References

[1] Budker, D.; Gawlik, W.; Kimball, D. F.; Rochester, S. M.; Yashchuk, V. V.; Weis, A. *Rev. Mod. Phys.* 2002, 74, 1153-1201.

[2] Hermann, G.; Scharmann, A. *Z. Phys.* 1968, 208, 367-380.

[3] Le Floch, A.; Le Naour, R. *Phys. Rev. A* 1971, 4, 290-295.

[4] Gawlik, W.; Kowalski, J.; Neumann, R.; Träger, F. *Opt. Commun.* 1974 12, 400-404.

[5] Barkov, L. M.; Melik-Pashayev, D. A.; Zolotorev, M. S. *Opt. Commun.* 1989, 70, 467-472.

[6] Budker, D.; Kimball, D. F.; Rochester, S. M.; Yashchuk, V. V.; Zolotorev, M. *Phys. Rev. A* 2000, 62, 043403.

[7] Budker, D.; Kimball, D. F.; Yashchuk, V. V.; Zolotorev, M. *Phys. Rev. A.* 2002, 65, 055403.

[8] Gawlik, W.; Krzemien, L.; Pustelny, S.; Sangla, D.; Zachorowski, J.; Graf, M.; Sushkov, A. O.; Budker, D. *Appl. Phys. Lett.* 2006, 88, 131108.

[9] Xu, S.; Donaldson, M. H.; Pines, A.; Rochester, S. M.; Budker, D.; Yashchuk, V. V. *Appl. Phys. Lett.* 2006, 89, 224105.

[10] Yashchuk, V. V.; Granwehr, J.; Kimball, D. F.; Rochester, S. M.; Trabesinger, A. H.; Urban, J. T.; Budker, D.; Pines, A. *Phys. Rev. Lett.* 2004, 93 160801.

[11] Xu, S.; Yashchuk, V. V.; Donaldson, M. H.; Rochester, S. M.; Budker, D.; Pines, A. *Proc. Nat. Acad. Sci. (USA)* 2006, 103, 12668-12671.

[12] Boyd, R. W. *Nonlinear Optics*, Academic Press, Amsterdam, 2003.

[13] Arimondo, E. In *Progess in Optics XXXV*, Elsevier Science, Edited by Wolf, E. 1996, 259-354.

[14] Harris, S. E. *Phys. Today* 1997, 50, 36-42.

[15] Akulshin, A. M.; Barreiro, S.; Lezama, A. *Phys. Rev. A* 1998, 57, 2996-3002.

[16] Rochester, S. M.; Budker, D. *Am. Journ. Phys.* 2001, 69, 450-454.

[17] Edmonds, A. R. *Angular Momentum in Quantum Mechanics*, Princeton University Press, Princeton, 1985.

[18] Nayak, N.; Agarwal, G. S. *Phys. Rev. A* 1985, 31, 3175-3182.

[19] Malakyan, Y. P.; Rochester, S. M.; Budker, D.; Kimball, D. F.; Yashchuk, V. V. *Phys. Rev. A.* 2004 69, 013817.

[20] Alexandrov, E. B.; Auzinsh, M.; Budker, D.; Kimball, D. F.; Rochester, S. M.; Yashchuk, V. V. *JOSA B* 2005, 22, 7-20.

[21] Benabid, F.; Knight, J. C.; Antonopoulos, G.; Russell, P. St. J. *Science* 2002, 298, 399-402.

[22] Light, P. S.; Benabid, F.; Couny, F.; Maric, M.; Luiten, A. N. *Opt. Lett* 2007, 32, 1323-1325.

[23] Hemmer, P. R.; Turukhin, A. V.; Shahriar, M. S.; Musser, J. A. *Opt. Express* 2001, 6, 361-363.

[24] Kanorsky, S. I.; Weis, A.; Skalla., J. *Appl. Phys. B* 1995, 60, S165-S168.

[25] Budker, D.; Hollberg, L.; Kimball, D. F.; Kitching, J.; Pustelny, S.; Yashchuk, V. V. *Phys. Rev. A* 2005, 71, 012903.

[26] Pustelny, S.; Jackson Kimball, D. F.; Rochester, S. M.; Yashchuk, V. V.; Budker, D. *Phys. Rev. A* 2006, 74, 063406.

[27] Kornack, T. W.; Smullin, S. J.; Lee, S.-K.; Romalis, M. V. *Appl. Phys. Lett* 2007, 90, 223501.

[28] Corney, A.; Kibble, B. P.; Series, G. W. *Proc. R. Soc. London, Ser. A* 1966, 70, 293-298.

[29] Wieman, C; Hänsch, T *Phys. Rev. Lett.* 1976, 36, 1170-1173.

[30] Bell, W.; Bloom, A. *Phys. Rev. Lett.* 1961, 6, 280-281.

[31] Corney, A.; Series, G. W. *Proc. Phys. Soc.* 1964, 83, 207-212.

[32] Pustelny, S.; Jackson Kimball, D. F.; Rochester, S. M.; Yashchuk, V. V.; Gawlik, W.; Budker, D. *Phys. Rev. A* 2006, 73, 023817.

[33] Budker, D.; Romalis, M. V. *Nat. Phys.* 2007, 3, 227-234.

[34] Bloom, A. L. *Appl. Opt.* 1962 1, 61-68.

[35] Dupont-Roc, J.; Haroche, S.; Cohen-Tannoudji, C. *Phys. Lett.* 1969, 28A, 638-639.

[36] Alexandrov, E. B.; Balabas. M. V.; Vershovski, A. K.; Pazgalev, A. S. *Tech. Phys.* 2004, 49, 779-783.

[37] Groeger, S.; Schenker, L. J.; Wynands, R.; Weis, A. *Euro. Phys. J. B* 2004, 33, 221-230.

[38] Kominis, I. K.; Kornack, T. W.; Allred, J. C.; Romalis, M. V. *Nature* 2003, 422, 596-599.

[39] Liew, L.-A.; Knappe, S.; Moreland, J.; Robinson, H.; Hollberg, L.; Kitching, J. *Appl. Phys. Lett.* 2004, 84, 2694-2696.

[40] Schwindt, P. D. D.; Knappe, S.; Shah, V.; Hollberg, H.; Kitching, J.; Liew, L.-A.; Moreland, J. *Appl. Phys. Lett.* 2004, 85, 6409-6411.

[41] Shah, V.; Knappe, S.; Schwindt, P. D. D.; Kitching, J. *Nat. Phot.* 2007, 1, 649-652.

[42] Taylor, J. M.; Cappellaro, P; Childress, L; Jiang, L; Budker, D; Hemmer, P. R.; Yacoby, A.; Walsworth, R.; Lukin, M. D. *Nature Phys.* 2008, 4, 810-816.

[43] Maze, J. R. ;Stanwix, P. L.; Hodges, J. S.; Hong, S.; Taylor, J. M.; Cappellaro, P.; Jiang, L.; Dutt, M. V. G.; Togan, E.; Zibrov, A. S.; Yacoby, A.; Walsworth, R. L.; Lukin, M. D. Nature 2008, 455, 644-647.

[44] Balasubramanian, G; Chan, I. Y.; Kolesov, R; Al-Hmoud, M.; Tisler, J.; Shin, C.; Kim, C.; Wojcik, A.; Hemmer, P. R.; Krueger, A.; Hanke, T.; Leitenstorfer, A.; Bratschitsch, R.; Jelezko, F.; Wrachtrup, J. *Nature* 2008, 455, 648-651.

[45] Budker, D.; Kimball, D. F.; Rochester, S. M.; Yashchuk, V. V.; Zolotorev, M. *Phys. Rev. A* 2000, 62, 043403.

[46] Allred, J. C.; Lyman, R. N.; Kornack, T. W.; Romalis, M. V. *Phys. Rev. Lett.* 2002, 89, 130801.

[47] Bechhoefer, J. *Rev. Mod. Phys.* 2005, 77, 783-836.

[48] Ledbetter, M. P., Acosta, V. M., Rochester, S. M., Budker, D.; Pustelny, S.; Yashchuk, V. V. *Phys. Rev. A* 2007, 75, 023405.

[49] Savukov, I. M.; Seltzer, S. J.; Romalis, M. V.; Sauer, K. L. *Phys. Rev. Lett.* 2005, 95, 063004.

[50] Alexandrov, E. B.; Balabas, M. V.; Kulyasov, V. N.; Ivanov, A. E.; Pazgalev, A. S.; Rasson, J. L.; Vershovski, A. K.; Yakobson, N. N. *Meas. Sci. Technol.* 2004, 15, 918-922.

[51] Seltzer, S.; Romalis, M. V. *Appl. Phys. Lett.* 2004, 85, 4804-4806.

[52] Pustelny, S.; Gawlik, W.; Rochester, S. M.; Jackson Kimball, D. F.; Yashchuk, V. V.; Budker, D. *Phys. Rev. A* 2006, 74, 063420.

[53] Bison, G.; Weis, A. *Phys. Rev. A* 2006, 74, 033401.

[54] Pustelny, S.; Wojciechowski, A.; Gring, M.; Zachorowski, A.; Gawlik, W. *J. Appl. Phys.* 2008, 103, 063108.

[55] Higbie, J. M.; Corsini, E.; Budker, D. *Rev. Sci. Instr.* 2006, 77, 113106.

[56] Pustelny, S.; Wojciechowski, A.; Kotyrba, M.; Sycz, K; Zachorowski, J.; Gawlik, W.; Cingoz, A.; Leefer, N.; Higbie, J. M.; Corsini, E.; Ledbetter, M. P.; Rochester, S. M.; Sushkov, A. O.; Budker, D. *Proc. of SPIE* 2007, 6604, 660404.

[57] Alexandrov, E. B.; Balabas, M. V.; Pasgalev, A. S.; Vershovskii, A. K.; Yakobson, N. N. *Laser Phys.* 1996, 6, 244-251.

[58] Blümich, B. *NMR Imaging of Materials*, Oxford University Press, Oxford, 2000.

[59] Tsukamoto, A.; Saitoh, K.; Suzuki, D.; Sugita, N.; Seki, Y.; Kandori, A.; Tsukada, K.; Sugiura, Y.; Hamaoka, S.; Kuma, H.; Hamasaki, N.; Enpuku, K. *IEEE Trans. Appl. Superconduc.* 2005, 15, 656-659.

[60] Wood, D. K.; Ni, K. K.; Schmidt, D. R.; Cleland, A. N. *Sens. Actuators, A* 2005, 120, 1-6.

[61] Pekas, N.; Porter, M. D.; Tondra, M.; Popple, A.; Jander, A. *Appl. Phys. Lett.* 2004, 85, 4783-4785.

[62] Xu, S.; Rochester, S. M.; Yashchuk, V. V.; Donaldson, M. H.; Budker, D. *Rev. Sci. Instrum.* 2006, 77, 083106.

[63] Nakagawa, T.; Tanaka, T.; Niwa, D.; Osaka, T.; Takeyama, H.; Matsunaga, T. *J. Biotechnol.* 2004, 118, 105-111.

[64] Balabas, M. V.; Budker, D.; Kitching, J.; Schwindt, P. D. D.; Stalnaker, J. E. *JOSA B* 2006, 23, 1001-1006.

[65] Wong-Foy, A.; Saxena, S.; Moule, A. J.; Bitter, H.-M. L.; Seeley, J. A.; McDermott, R.; Clarke, J.; Pines, A. *J. Magn. Reson.* 2002, 157, 235-241.

[66] Moule, A. J.; Spence, M. M.; Han, S.; Seeley, J. A.; Pierce, K. L.; Saxena, S.; Pines, A. *Proc. Natl. Acad. Sci. (USA)* 2003, 100, 9122-9127.

[67] Seeley, J. A.; Han, S.; Pines, A. *J. Magn. Reson.* 2004, 167, 282-290.

[68] Yashchuk, V. V.; Budker, D.; Gawlik, W.; Kimball, D. F.; Malakyan, Y. P.; Rochester, S. M. *Phys. Rev. Lett.* 2003, 90, 253001.

[69] Acosta, V.; Auzinsh, M.; Gawlik, W.; Grisins, P.; Higbie, J. M.; Jackson Kimball, D. F.; Krzemień, L.; Ledbetter, M. P.; Pustelny, S.; Rochester, S. M.; Yashchuk, V. V.; Budker, D. *Opt. Express* 2008, 16, 11423-11430.